Journal of Colloid and Interface Science 690 (2025) 137337

Contents lists available at ScienceDirect

Journal of Colloid And Interface Science

journal homepage: www.elsevier.com/locate/jcis

Regular Article

Copper/calcium co-doped carbon dots for targeted cancer therapy with dual-mode imaging and synergistic induction of cuproptosis and calcium-mediated apoptosis

Wenqian Zheng [a], Yang Liu [a], Jinru Liu [a], Yuping Zhao [a], Peiyu Wang [a], Yi Wang [b], Yuxuan Wang [a], Zeyu Lu [a], Xiaofan Liu [a], Yaru Shi [a], Na Zhou [c], Fermín Eduardo González [d], Hongchen Sun [a], Ding Zhou [a,*], Xiaowei Xu [a,*]

[a] Jilin Provincial Key Laboratory of Tooth Development and Bone Remodeling, Hospital of Stomatology, Jilin University, Changchun 130021, PR China
[b] Graduate Program in Applied Physics, Northwestern University, Evanston, IL 60208, USA
[c] School of Pharmacy, State Key Laboratory of Quality Research in Chinese Medicines and Laboratory of Drug Discovery from Natural Resources and Industrialization, Macau University of Science and Technology, Macau 999078, PR China
[d] Laboratory of Experimental Immunology & Cancer, Faculty of Dentistry, University of Chile, Santiago 8380492, Chile

GRAPHICAL ABSTRACT

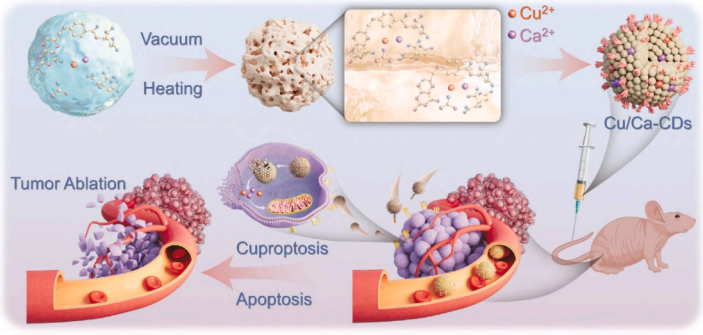

ARTICLE INFO

Keywords:
Carbon dot
Cuproptosis
Calcium overload
Dual-mode imaging
Tumor-targeted therapy

ABSTRACT

Squamous cell carcinoma remains a highly aggressive malignancy with persistently high global incidence and mortality rates, posing significant challenges for effective treatment. Traditional chemotherapies lack specificity, leading to damage in normal tissues and severe side effects, highlighting the urgent need for targeted therapeutic strategies. In this study, copper and calcium co-doped carbon dots (Cu/Ca-CDs) were synthesized using a vacuum-confined heating method. These Cu/Ca-CDs demonstrated excellent tumor-targeting ability through specific binding to folate receptors on murine squamous cell carcinoma cell line (SCC7), facilitated by their pterin ring structure. Mechanistic studies revealed that Cu/Ca-CDs induced SCC7 tumor cell death through copper-induced cuproptosis and calcium overload-mediated apoptosis, as confirmed by Western blot, immunofluorescence staining, and Rhod-2 calcium probe analyses. The dual-mode imaging capability of Cu/Ca-CDs, enabled by fluorescence and computed tomography properties, allowed for real-time tracking of their distribution and

* Corresponding authors.
E-mail addresses: zhouding@jlu.edu.cn (D. Zhou), xiaoweixu@jlu.edu.cn (X. Xu).

https://doi.org/10.1016/j.jcis.2025.137337
Received 13 January 2025; Received in revised form 7 March 2025; Accepted 14 March 2025
Available online 17 March 2025

accumulation within tumors. This imaging-guided approach ensured precise delivery to tumor tissues while minimizing damage to normal tissues. *In vivo* experiments demonstrated significant tumor volume reduction and increased survival rates in tumor-bearing mice treated with Cu/Ca-CDs, without any observed toxicity to normal tissues or changes in body weight, underscoring the efficacy and biosafety of Cu/Ca-CDs. These findings highlight Cu/Ca-CDs as a promising strategy for precision oncology, offering effective tumor targeting, dual-mode imaging, and synergistic anti-tumor efficacy with reduced side effects.

1. Introduction

Squamous cell carcinoma (SCC) represents a major category of malignant tumors arising from squamous epithelial cells, affecting various organs including the head and neck, lung, esophagus, and skin [1–3]. This aggressive malignancy is characterized by rapid proliferation, high invasiveness, and frequent metastasis, making it one of the leading causes of cancer-related mortality worldwide [4,5]. Despite significant advances in cancer treatment modalities, including surgery, radiotherapy, and chemotherapy, the management of SCC remains challenging due to its heterogeneous nature and resistance to conventional therapies [6]. Traditional chemotherapeutic approaches, while effective in killing cancer cells, lack specificity in their targeting mechanism, resulting in significant damage to healthy tissues and severe side effects [7,8]. This lack of precision highlights the urgent need for novel therapeutic agents capable of selectively targeting tumor cells while minimizing harm to healthy tissues.

In recent years, cuproptosis has garnered significant attention as a novel form of regulated cell death, distinct from traditional programmed cell death [9–11]. Cuproptosis is induced by the intracellular accumulation of copper ions, which bind to lipoylated dihydrolipoamide S-acetyltransferase (DLAT) in the tricarboxylic acid (TCA) cycle, leading to DLAT aggregation and mitochondrial dysfunction [12–14]. Copper ions also downregulate iron-sulfur (Fe-S) cluster proteins, collectively inducing protein toxicity stress and triggering cell death [15,16]. Similarly, calcium ions can also induce apoptosis through mitochondrial dysfunction caused by calcium overload [17,18]. While calcium ions are essential intracellular signaling molecules, an abnormal increase in their concentration disrupts mitochondrial membrane potential, activating mitochondria-mediated apoptotic pathways and ultimately causing cell death [19,20]. Although cuproptosis and calcium overload-mediated apoptosis show great potential as emerging cancer treatment strategies, their current lack of precise targeting limits their direct clinical application.

Carbon dots (CDs), a class of carbon-based nanomaterials, exhibit significant potential in biomedical applications due to their small size, excellent cellular permeability, fluorescence properties, and tunable surface functionalization [21,22]. By modulating precursor types and synthesis conditions, CDs can be engineered to possess specific physiological functions such as tumor targeting and drug delivery capabilities [23,24]. In this study, copper and calcium co-doped CDs (Cu/Ca-CDs) were synthesized using a vacuum-confined heating method. These Cu/Ca-CDs demonstrated excellent tumor-targeting ability, dual-mode fluorescence/computed tomography (CT) imaging capability, and significant anti-tumor efficacy. The presence of a pterin ring structure enables specific binding to folate receptors on tumor cells, facilitating selective uptake [25,26]. Mechanistic studies revealed that Cu/Ca-CDs induce SCC7 tumor cell death through copper-induced cuproptosis and calcium overload-mediated apoptosis, as confirmed by *in vitro* experiments. Furthermore, the dual-mode imaging capability of Cu/Ca-CDs allowed real-time tracking of their distribution and accumulation within tumors, providing a precise and guided therapeutic approach. *In vivo* studies further demonstrated significant tumor volume reduction and increased survival rates in tumor-bearing mice. These findings underscore the potential of Cu/Ca-CDs as a promising strategy for precision oncology, offering effective tumor targeting, reduced toxicity to normal tissues, and potent anti-tumor effect (Scheme 1).

2. Materials and methods

2.1. Materials

Citric acid (99.5 %), folic acid (HPLC, 97 %), anhydrous calcium chloride ($CaCl_2$, 96 %), 3,3′,5,5′-Tetramethylbenzidine (TMB, 99 %) and hydrogen peroxide (H_2O_2) were purchased from Aladdin. Copper (II) chloride dihydrate ($CuCl_2{\cdot}2H_2O$, AR) and urea (AR, 99 %) were obtained from Macklin. Hydrochloric acid was procured from Beijing Chemical Factory. The Spectra/Por® Biotech Grade Cellulose Ester Dialysis Membrane (MWCO: 100–500 D) was sourced from Spectrum Laboratories (Rancho Dominguez, CA). Roswell Park Memorial Institute (RPMI) 1640 medium without Calcium Nitrate, containing 2.05 mM L-Glutamine, and Dulbecco's modified Eagle medium (DMEM) with high glucose were purchased from Hyclone (Logan, UT, USA) Fetal Bovine Serum (FBS) was obtained from Biological Industries (Cromwell, CT, USA).

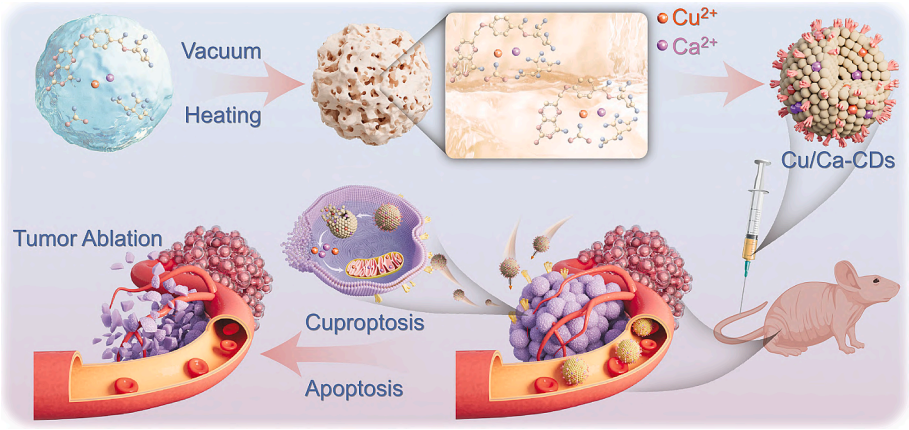

Scheme 1. Schematic illustration of the synthetic process of Cu/Ca-CDs and the mechanisms of tumor ablation induced by Cu/Ca-CDs.

2.2. Synthesis and purification of Cu/Ca-CDs

Initially, 0.2 g of folic acid, 0.5 g of citric acid, 1.0 g of urea, 0.5 g of $CuCl_2{\cdot}2H_2O$, and 1.0 g of $CaCl_2$ were dissolved in 3 mL of deionized water. The solution was then heated to 120 °C in an oven. Under vacuum conditions, the temperature was further increased to 250 °C and maintained for 1 h, with a vacuum pressure of approximately 1 Pa provided by a mechanical vacuum pump. This process yielded inflated foams containing Cu/Ca-CDs, which could be easily ground into a powder. The as-prepared powder was dissolved in a dilute hydrochloric acid solution, followed by centrifugation at 10,000 rpm for 10 min to remove larger aggregated particles. Subsequently, the Cu/Ca-CDs solution was dialyzed in deionized water for 72 h using a dialysis bag to eliminate unreacted materials and small molecular by-products. Finally, the purified Cu/Ca-CDs solution was freeze-dried, and the Cu/Ca-CDs could be re-dissolved in deionized water at the required concentration for subsequent experiments. The singly doped Cu-CDs and Ca-CDs, as well as the CDs without Cu and Ca doping, were prepared using the same method by removing the corresponding precursor materials accordingly.

2.3. Characterization of Cu/Ca-CDs

Photoluminescence (PL) spectroscopy was conducted with a Shimadzu RF-5301 PC spectrophotometer. Ultraviolet–visible (UV–vis) absorption spectra were measured using a Lambda 800 UV–vis spectrophotometer. The zeta potential of the CDs was analyzed using dynamic light scattering (DLS) (Zetasizer NanoZS, Malvern Instruments, Britain) at a neutral pH and room temperature. Fourier transform infrared (FTIR) spectra were obtained using a Bruker VERTEX 80 V instrument. High-resolution transmission electron microscopy (HRTEM) image was performed with a JEOL JEM-2100F electron microscope. Energy dispersive spectra (EDS) were collected using an Inca X-Max instrument (Oxford Instruments). X-ray photoelectron spectroscopy (XPS) was conducted using the NEXSA system from Thermo Scientific.

2.4. Catalytic activity of Cu/Ca-CDs

Using TMB as a probe, the catalytic activity of Cu/Ca-CDs and CDs in the presence of H_2O_2 was studied. Cu/Ca-CDs solution was mixed with TMB and H_2O_2, and the UV–Vis absorption spectra of the resulting solution were measured. Control solutions, including solely H_2O_2, TMB, Cu/Ca-CDs, H_2O_2 + TMB, Cu/Ca-CDs + H_2O_2, and Cu/Ca-CDs + TMB, were also tested under the same conditions. The UV–vis absorption spectra of these solutions were measured at 652 nm.

2.5. The photothermal activity of Cu/Ca-CDs

Place an appropriate amount of Cu/Ca-CDs solution in a quartz cuvette, ensuring the solution is well-dispersed. Irradiate the solution with 405 nm and 808 nm lasers, using a controlled light source. During the irradiation, continuously monitor the temperature changes of the solution using a digital thermometer and record the temperature data at 0, 1, 2, 3, 4, and 5 min to ensure accurate temperature measurement. The laser power should remain consistent throughout the experiment, and the experimental environment should be kept at room temperature to minimize external interference.

2.6. Cell culture

Murine squamous cell carcinoma cell line (SCC7) was cultured in RPMI 1640 medium supplemented with 10 % FBS, 100 U/mL penicillin, 100 μg/mL streptomycin, and 25 μg/mL Amphotericin B solution in a 5 % CO_2 humidified incubator at 37 °C. The culture medium was changed every 1 day. Mouse fibroblast cells (L929) were resuspended in DMEM high glucose medium supplemented with 10 % FBS and cultured in an incubator at 37 °C with 5 % CO_2. The culture medium was changed every 1 day.

2.7. Cell targeting and immunofluorescence staining

SCC7 cells were seeded at a density of 1×10^4 cells per well in confocal dishes and incubated overnight at 37 °C in a 5 % CO_2 atmosphere. The cells were divided into two groups for targeting assessment: 1) Cu/Ca-CDs and 2) folic acid + Cu/Ca-CDs. After incubation for 0 to 120 min, the culture medium was aspirated at different time points (60 and 120 min), and the cells were washed three times with PBS. Finally, fluorescence intensity was observed using a confocal laser scanning microscope (CLSM). After overnight culture in RPMI 1640 medium containing Cu/Ca-CDs, the cells were fixed in 4 % paraformaldehyde fixative for 20 min, permeabilized with 0.1 % Triton X-100 for 10 min, and blocked with goat serum at room temperature for 30 min. The blocking solution was discarded, and DLAT (1:250, Proteintech) was added and incubated overnight at 4 °C. After bringing to room temperature, cells were incubated with CoraLite594-conjugated Goat Anti-Rabbit IgG (H + L) (1:200, Proteintech) in the dark at room temperature for 2 h, followed by DAPI staining for 5 h. Finally, cells were imaged using CLSM.

2.8. Cytotoxicity assays

For the cytotoxicity assays, a 96-well plate was prepared with blank control wells and various concentrations of Cu/Ca-CDs (0, 100, 200, 300, 400 μg/mL). Except for the blank group, each well received 100 μL of SCC7 cell suspension (2,000 cells). After incubating for 24 h at 37 °C in a 5 % CO_2 humidified environment, the original medium was discarded, and 100 μL of different concentrations of Cu/Ca-CDs was added to each well. The cells were then incubated for another 6, 12, and 24 h under the same conditions. Following this, the original medium was removed, and each well received 10 μL of CCK-8 solution and 90 μL of serum-free RPMI 1640 medium, incubating for approximately 1 h. The absorbance at 450 nm was measured using a BioTek Synergy HT Multi-Mode Microplate Reader. The OD values of the test wells were adjusted by subtracting the blank OD value, and the mean ± SD of each set was calculated. The cell viability percentage was calculated as follows: cell viability (%) = (OD of treatment group / OD of control group) × 100 %. The same experimental setup was used to detect the cytotoxicity on L929 cells.

SCC7 cells were also seeded at 2×10^5 cells per well in a 6-well plate and incubated for 24 h. After this period, 3 mL of RPMI 1640 medium containing various concentrations of Cu/Ca-CDs (0, 100, 200, 300, 400 μg/mL) was added to each well. After another 24 h, cells were digested using trypsin, centrifuged at 4 °C, and collected into 1.5 mL EP tubes. The cells were washed twice with pre-chilled phosphate buffer saline (PBS) at 1,500 rpm for 5 min. Finally, the cells were stained according to the manufacturer's instructions using the Annexin V-FITC/7-AAD apoptosis assay kit (Tianjin Simu Biotech Co., Tianjin, China), followed by flow cytometry analysis to detect fluorescence signals.

SCC7 cells were plated in small dishes and cultured overnight. The medium was then replaced with 3 mL of RPMI 1640 medium containing varying concentrations of Cu/Ca-CDs (0, 100, 200, 300, 400 μg/mL). After 24 h, the medium was removed, and cells were washed with PBS once. A working solution of propidium iodide detection was added (1 mL), and the cells were incubated in the dark at 37 °C for 30 min. After incubation, the staining effect was observed under a fluorescence microscope.

2.9. Molecular dynamics (MD) simulations

The folate receptor protein structure was obtained from the UniProt protein database (ID: P35846). A basic model of Cu/Ca-CDs was created using HRTEM and XPS analyses, then optimized through density functional theory methods. MD simulations were executed using the

GROMACS package, version 2018.8, with the AMBER99SB-ILDNP force field for all-atom simulations. The Antechamber program, utilizing the General Amber force field (GAFF), generated the force field parameters for Cu/Ca-CDs. To solvate the system within a cubic box, TIP3P water molecules were added, ensuring a minimum distance of 10 Å from the protein to the box boundary. Excess charges in the system were neutralized using Na^+ ions. Periodic boundary conditions were applied in all directions to model an infinite system. To prevent negative interactions, steepest descents and/or conjugate gradient minimization were carried out with a tolerance of 1,000 kJ/mol/nm. Following this, a two-phase equilibration was performed before production simulations. Initially, the system underwent a constant volume (NVT) ensemble simulation at 300 K for 1 ns using the V-rescale method. The equilibrated structures from the NVT stage were then subjected to a constant pressure (NPT) equilibration for another 1 ns using the Parrinello-Rahman barostat, maintaining an isotropic pressure of 1.0 bar. Production MD simulations lasted 120 ns without any restraints, and simulation trajectories were recorded every 10 ps for subsequent analysis of root mean square deviation (RMSD), root mean square fluctuation (RMSF), and protein–ligand interactions.

2.10. Measurement of intracellular Ca^{2+}

SCC7 cells were plated in confocal dishes at a density of 1×10^5 cells per well and incubated for 24 h. The cells were then treated with PBS or Cu/Ca-CDs for 0, 2, and 4 h, respectively. To visualize the distribution of cytoplasmic Ca^{2+}, cells were washed twice with PBS, incubated with Rhod-2 AM (5 μM) for 30 min, and subsequently imaged using CLSM.

2.11. Reverse transcriptase quantitative polymerase chain reaction (RT-qPCR) assay

SCC7 cells were divided into two groups for RT-qPCR assays: 1) PBS and 2) Cu/Ca-CDs. After 12 h of incubation, total RNA was extracted from the SCC7 cells using a Quick RNA Extraction Kit. Subsequently, cDNA was synthesized using a cDNA Reverse Transcription Kit. Quantitative real-time PCR was performed on a StepOnePlus Real-Time PCR system. The PCR cycling conditions consisted of an initial denaturation step at 95 °C for 5 min, followed by 40 cycles of denaturation at 95 °C for 10 s and annealing/extension at 60 °C for 30 s. The relative gene expression was calculated using the ΔΔCt method, with the ACTB gene serving as an internal reference. The primer sequences were provided in Table S1.

2.12. Western blot

SCC7 cells were also divided into two groups for Western blot assays: 1) PBS and 2) Cu/Ca-CDs. Following a 12-hour incubation, cell lysates were collected to extract proteins. The proteins were extracted by centrifugation at 14,000 rpm for 30 min using a BCA protein assay kit (P0010, Beyotime). Each lane received 30 μg of protein samples, which were then separated using 10 % sodium dodecyl sulfate–polyacrylamide gel electrophoresis (SDS-PAGE) and transferred to a PVDF membrane using a gel-electrophoretic apparatus (Bio-Rad mini, USA). The membranes were blocked with 5 % milk for 2 h, followed by three washes. The membranes were incubated overnight at 4 °C with primary antibodies: DLAT (1:5,000, Proteintech), LIAS (1:2,000, Proteintech), FDX1 (1:5,000, Abcam), Bax (1:5,000, Proteintech), Bcl-2 (1:5,000, Proteintech), Caspase 9 (1:500, Proteintech) and Caspase 3 (1:1,000, Proteintech). After washing the membranes three times, they were incubated at room temperature for 2 h with HRP-conjugated Affinipure Goat Anti-Rabbit IgG (H + L) (1:10,000, Proteintech). Western blot images were captured using a gel imaging system after applying 200 μL of ECL chemiluminescent reagent (PK10002, Proteintech) to the membrane. GAPDH (1:10,000, Proteintech) was used as a loading control.

2.13. Mitochondrial membrane potential detection

The mitochondrial membrane potential was assessed using the Mitochondrial Membrane Potential Assay Kit with JC-1 (C2006, Beyotime). SCC7 cells were divided into three groups for this analysis: 1) PBS, 2) Cu/Ca-CDs, and 3) CCCP (positive control). After removing the culture medium, the cells were washed three times with PBS and then incubated with JC-1 staining solution for 20 min at 37 °C in a 5 % CO_2 atmosphere. Finally, the supernatant was discarded, and the cells were washed twice with JC-1 buffer. Fluorescence was observed using CLSM. The calculation was performed using the open-source software ImageJ. To minimize statistical errors, images with consistent capturing parameters were selected. These images were then opened in ImageJ, and the "split channels" function under the "Color" menu was used to separate the red and green channels. Next, the "Set Measurements" option under the "Analyze" menu was used to measure the Mean Gray Value for both red and green channels. The red and green fluorescence intensities were then divided to calculate the red/green ratio.

2.14. Animal experiments

All animal experiments were conducted in accordance with the Guidelines for Animal Care and Use of Jilin University and were approved by the Animal Ethics Committee of Jilin University (approval number: 2024–05-010). The SCC7 tumor-bearing mice model was established by subcutaneously injecting SCC7 cells (1×10^7 cells in 100 μL of suspension) into the left flank of mice. When the tumor volumes reached approximately 100 mm^3, the female Balb/c nude mice were randomly divided into two groups (n = 5 mice per group): the PBS group and the Cu/Ca-CDs group. All mice were housed under standard laboratory conditions with a controlled temperature of 22 °C, a humidity level of 50 %, and a 12-hour light/dark cycle throughout the experiment. The Cu/Ca-CDs group received tail vein injections of Cu/Ca-CDs solution (10 mg/kg) on days 0, 2, 4, and 6, while the PBS group received equal volumes of PBS at the same time points. To accurately evaluate the therapeutic effects, tumor volume (V) was calculated using the formula $V = (Width^2 \times Length) / 2$. Tumor volume changes were recorded before and after each injection, and body weight was monitored regularly to assess the health status and potential side effects. After two weeks, the mice were sacrificed to assess therapeutic efficacy and safety. Tumor tissues were collected, and the final tumor weights were recorded. Additionally, the survival rate of the animals was tracked over a 60-day period to evaluate the long-term effects of different treatments on survival.

For histological analysis, the main organs-including the heart, liver, spleen, lung, and kidney-and tumor tissues were collected at the end of the treatment and fixed in 4 % paraformaldehyde solution. The tissues were then processed to prepare paraffin sections, which were stained with hematoxylin and eosin (H&E) and observed under an optical microscope to evaluate morphological changes and identify any treatment-related toxicity or damage. Furthermore, to further evaluate tumor cell apoptosis, tumor sections were stained using a terminal deoxynucleotidyl transferase-mediated dUTP nick-end labeling (TUNEL) assay kit to detect the presence and quantity of apoptotic cells. Additionally, Alizarin Red S staining was performed on tumor sections to observe potential calcification. All experimental results, including tumor volume, histological changes, and apoptosis analysis, will be comprehensively analyzed to assess the therapeutic efficacy of Cu/Ca-CDs and their potential side effects.

2.15. In vivo fluorescence and CT imaging

Female Balb/c mice bearing SCC7 tumors were chosen for both fluorescence and CT imaging studies. Cu/Ca-CDs were injected intratumorally, and the mice underwent two-dimensional fluorescence imaging at intervals of 0, 15, 30, 45, and 60 min using a NIR-II-Integration

system (Digi-United biotech). The fluorescence intensity was subsequently assessed. For CT imaging, Cu/Ca-CDs were also injected intratumorally, and CT scans were performed at the same time points (0, 15, 30, 45, and 60 min) using a CT scanner (United-Imaging, uCT 760). Quantitative analysis of the CT values was then carried out.

2.16. Hemolysis assay

Fresh whole blood was obtained from healthy mice and collected into heparinized centrifuge tubes. The blood was centrifuged at 1,500 rpm for 10 min to separate red blood cells (RBCs) from plasma. The supernatant was discarded, and the RBCs were washed three times with physiological saline. A 5 % RBCs suspension was prepared using saline. Negative control (RBCs suspension + saline), positive control (RBCs suspension + Triton X-100), and sample group (RBCs suspension + Cu/Ca-CDs) were set up and incubated at 37 °C for 1 h. After incubation, the mixtures were centrifuged at 1,500 rpm for 10 min to separate the RBCs from the supernatant. The supernatant was transferred to a 96-well plate, and the absorbance at 540 nm was measured using a microplate reader. The percentage of hemolysis was calculated using the equation: Hemolysis (%) = ((OD sample − OD negative control)/(OD positive control − OD negative control)) × 100 %.

2.17. Inductively coupled plasma mass spectrometry (ICP-MS) metabolism analysis

To investigate the *in vivo* metabolism of Cu/Ca-CDs, ICP-MS was used to analyze the copper and calcium content in organs, tumors, and excretions at different time points. Mice were randomly divided into six groups (n = 3 per group), including the control group (PBS injection) and the Cu/Ca-CDs-treated groups at different time points (0, 6, 12, 24, and 48 h). At each designated time point, mice were anesthetized, and samples from the heart, liver, spleen, lungs, kidneys, and tumor tissues were collected, along with urine and feces. All tissue samples were digested using concentrated nitric acid for 120 min to ensure complete decomposition of organic matter and the release of Cu and Ca elements. The copper and calcium concentrations in the organs and excreta were then measured using ICP-MS to evaluate the biodistribution, metabolism, and excretion of Cu/Ca-CDs. This study provides insights into the retention time, biodistribution, and potential biosafety concerns of Cu/Ca-CDs *in vivo*.

2.18. Immunohistochemistry assay

First, antigen retrieval was performed on paraffin-embedded slides for 30 min using a Pepsin Antigen Retrieval Kit. Endogenous peroxidase activity was then blocked with 3 % H_2O_2 for 10 min at room temperature. After washing with PBS, the slides were blocked with 10 % normal goat serum at 37 °C for 1 h. Subsequently, the slides were incubated overnight at 4 °C with primary antibodies: DLAT (1:1,000) and FDX1 (1:100). After three washes with PBS for 10 min each, a reaction enhancer was added, and the slides were incubated at 37 °C for 20 min, followed by PBS washing. An HRP-conjugated goat anti-mouse/rabbit IgG polymer was then added, and the slides were incubated at 37 °C for another 20 min before washing again with PBS. The slides were stained with DAB peroxidase substrate and counterstained with hematoxylin. After dehydration through graded alcohols, the slides were mounted with neutral balsam. Finally, the specimens were observed under an optical microscope.

2.19. Statistical analysis

Measurements were repeated three times, and the standard deviation was plotted as error bars. Statistical analysis was performed using one-way ANOVA, with a *P*-value of < 0.05 considered to indicate statistical significance.

3. Results and discussion

3.1. Synthesis and characterization of Cu/Ca-CDs

Using our previously developed space-confined vacuum heating method [27], Cu/Ca-CDs with tumor-targeting ability were synthesized from folic acid, citric acid, urea, $CuCl_2{\cdot}2H_2O$, and $CaCl_2$. After dissolving the precursors, the solution was heated under vacuum, gradually inflating into a spherical porous foam structure, effectively confining the copper and calcium elements within the foam walls. As the temperature increased, the precursors underwent dehydration and carbonization, resulting in a crude product containing CDs (Fig. 1a). Under daylight, this spherical product appeared brownish, and its porous structure was clearly visible (Fig. 1b). The crude product was purified by dissolution, centrifugation, and dialysis, yielding a Cu/Ca-CDs solution that appeared yellow under sunlight and exhibited bright green fluorescence under UV light (Fig. 1c). The UV–vis absorption spectrum of Cu/Ca-CDs displayed an absorption peak at 405 nm (Fig. 1d). The PL spectrum of Cu/Ca-CDs showed an emission peak at 530 nm, providing a unique visualization method for tracking the distribution and behavior of Cu/Ca-CDs in biological systems (Fig. 1d). To evaluate whether the fluorescence properties of Cu/Ca-CDs could be safely used for bioimaging without causing thermal damage to surrounding tissues under excitation, the photothermal activity of Cu/Ca-CDs was examined. As shown in Fig. S1, Cu/Ca-CDs exhibited no detectable photothermal activity. This is primarily because, when excited by incident light, electrons in Cu/Ca-CDs primarily return to the ground state *via* radiative transitions rather than non-radiative processes. Moreover, the consistent PL peak position under different excitation wavelengths indicated uniform particle size (Fig. S2), further confirmed by HRTEM. The HRTEM images revealed well-dispersed Cu/Ca-CDs with a uniform average diameter of 4.5 nm (Fig. 1e). The lattice spacing was measured as 0.21 nm (Fig. 1f), consistent with the (1 0 0) crystallographic facet of graphitic carbon, suggesting a graphene-like conjugated structure [28,29]. To further elucidate the formation mechanism and chemical structure of Cu/Ca-CDs, FTIR and XPS analyses were conducted.

The FTIR spectrum of citric acid exhibited two strong absorption peaks at 1751 cm^{-1} and 1712 cm^{-1}, corresponding to the C═O stretching vibrations of free carboxyl groups and hydrogen-bonded carboxyl groups, respectively (Fig. 1g). An absorption band in the range of 3080–3580 cm^{-1} was attributed to the O—H stretching vibration of carboxyl groups. These peaks confirm the presence of carboxyl groups. The FTIR spectrum of urea displayed characteristic amine group vibrations, including an N—H antisymmetric stretching vibration at 3347 cm^{-1}, and an N—H bending vibration at 1620 cm^{-1}. The presence of carboxyl and amino groups in the precursors facilitated dehydration, condensation, and carbonization, leading to the formation of Cu/Ca-CDs. In the FTIR spectrum of folic acid, an absorption peak at 1610 cm^{-1} corresponded to the C═N stretching vibration of the isonitrile group in the pterin ring, while a peak at 1412 cm^{-1} was attributed to the C═N stretching vibration of the nitrogen-containing heteroaromatic group. These peaks confirmed the presence of a pterin ring structure, which facilitates binding to folate receptor proteins on tumor cells. The FTIR spectrum of Cu/Ca-CDs exhibited a broad band in the 1500–1770 cm^{-1} range, which could be deconvoluted into four distinct peaks (Fig. 1h). These peaks included the C═O stretching vibration of carboxyl groups at 1712 cm^{-1}, the C═O stretching vibration corresponding to the amide I band at 1673 cm^{-1}, the N—H bending vibration associated with the amide II band at 1550 cm^{-1}, and the C═N stretching vibration of isonitrile groups at 1619 cm^{-1}. The presence of amide bonds in Cu/Ca-CDs indicated their formation *via* dehydration condensation between carboxyl and amino groups [30]. Additionally, the isonitrile and nitrogen heteroaromatic groups at 1619 cm^{-1} and 1412 cm^{-1} confirmed the presence of pterin ring structures, enabling targeted binding to tumor cells.

XPS characterization further supported these findings. The C 1 s

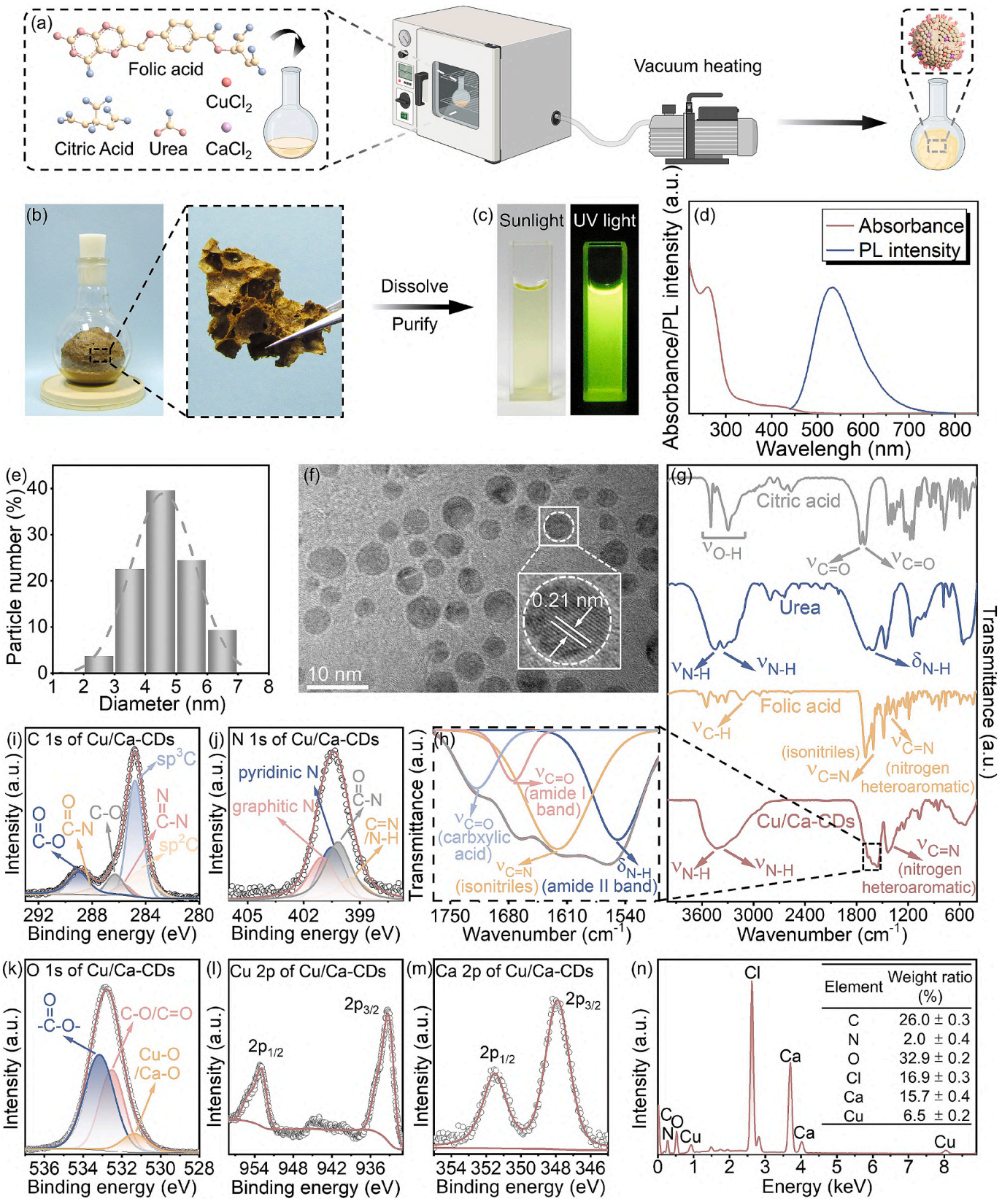

Fig. 1. Characterization of Cu/Ca-CDs. (a) Schematic diagram of Cu/Ca-CDs synthesis. (b) Photographs of crude product containing Cu/Ca-CDs (left panel) and a locally enlarged image (right panel). (c) Cu/Ca-CDs solution taken under sunlight and UV light, respectively. (d) PL emission (red line) spectra of the Cu/Ca-CDs solution. (e) The corresponding particle size distribution histogram of Cu/Ca-CDs. (f) HRTEM image of Cu/Ca-CDs, with an inset showing an enlarged view of the Cu/Ca-CDs lattice. (g) FTIR spectra of citric acid (gray line), urea (blue line), folic acid (yellow line) and Cu/Ca-CDs (red line). (h) The enlarged image shows the peak fitting of the FTIR spectra of Cu/Ca-CDs in the 1500–1770 cm^{-1} range. High-resolution XPS spectra of Cu/Ca-CDs: (i) C 1s, (j) N 1s, (k) O 1s, (l) Cu 2p and (m) Ca 2p. (n) EDS spectrum of Cu/Ca-CDs. The inset of (n) is a table showing the weight ratios of the elements in Cu/Ca-CDs. Data are presented as mean from three independent experiments. (For interpretation of the references to color in this figure legend, the reader is referred to the web version of this article.)

spectrum of citric acid showed four peaks, which included sp^2 C (284.6 eV), sp^3 C (285.2 eV), C—O (286.2 eV), and –COO– (288.5 eV). The O 1 s spectrum exhibited peaks at 532.2 eV and 533.2 eV, corresponding to O—H and C═O groups, respectively (Fig. S3). The N 1 s spectrum of urea confirmed the presence of amino groups (Fig. S4). These findings aligned with the FTIR results, indicating that carboxyl and amino groups participated in the formation of Cu/Ca-CDs *via* dehydration condensation. The C 1 s spectrum of folic acid was deconvoluted into five peaks corresponding to sp^2 C (284.6 eV), sp^3 C (285.2 eV), N═C-N (286.0 eV), –CON- (287.9 eV), and –COO- (288.5 eV) (Fig. S5). The N 1 s spectrum exhibited peaks at 399.1 eV (*N*-C═N/N—H), 400.1 eV (–CON-), and 400.5 eV (pyridinic N). These results confirmed the presence of the pterin ring structure. The full XPS spectrum of Cu/Ca-CDs indicated the presence of C, N, O, Cu, and Ca, confirming successful doping (Fig. S6). Detailed analysis of the C 1 s spectrum revealed a peak at 287.9 eV corresponding to the amide bond (–CON-), which was consistent with the FTIR results, and a peak at 286.0 eV attributed to N═C-N (Fig. 1i). The N 1s spectrum revealed peaks at 399.3 eV (C═N/N—H), 400.1 eV (–CON–), 400.5 eV (pyridinic N), and 401.1 eV (graphitic N), indicating the incorporation of pterin rings in Cu/Ca-CDs (Fig. 1j). Compared to the O 1 s spectrum of the raw materials, the Cu/Ca-CDs spectrum contained peaks at 532.2 eV for C—O/C═O and 533.2 eV for –COO- [31]. Notably,

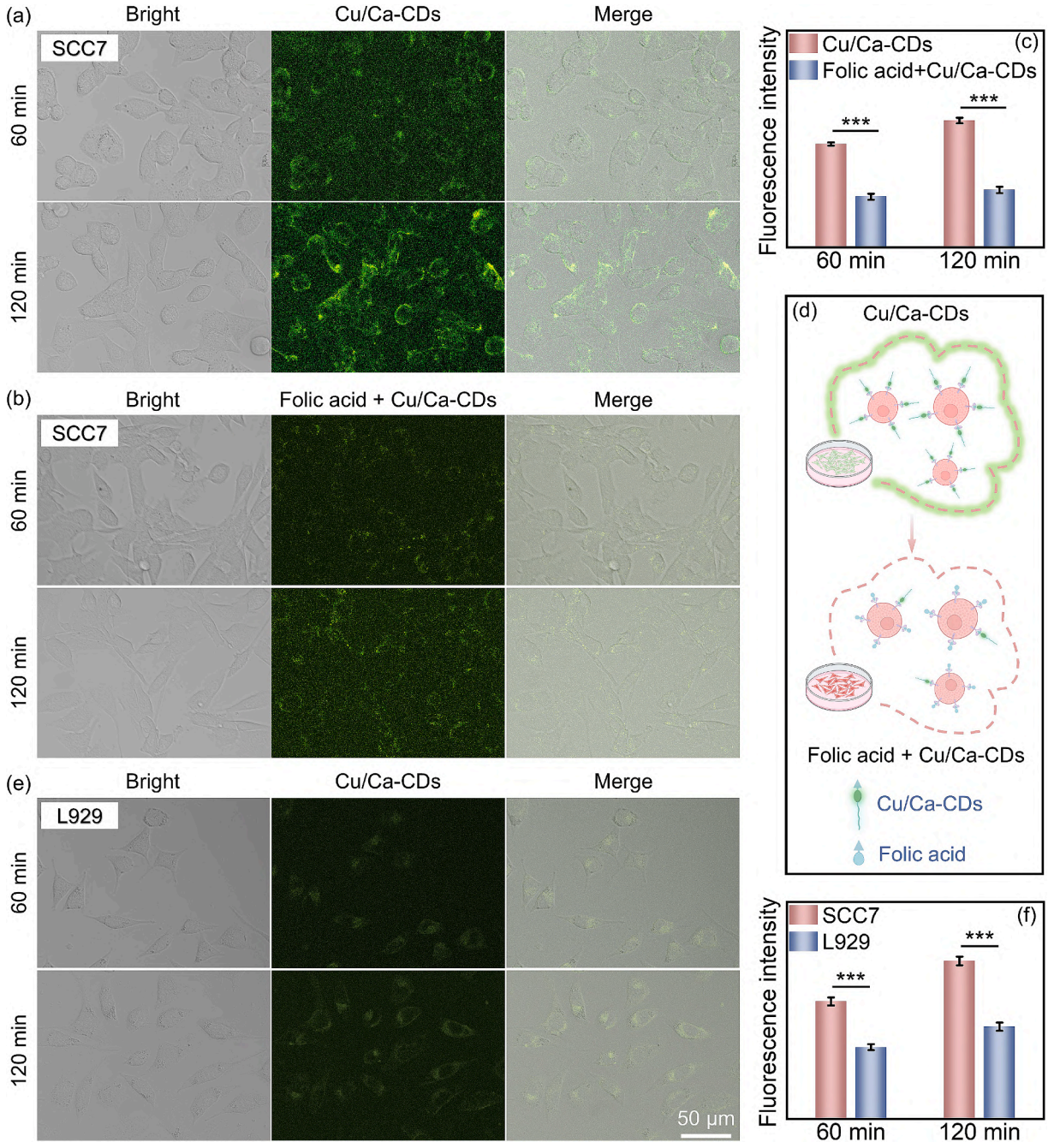

Fig. 2. Tumor-targeting ability of Cu/Ca-CDs. (a) The enrichment ability of Cu/Ca-CDs in SCC7 cells. (b) The enrichment ability of Cu/Ca-CDs in SCC7 cells treated with folic acid. (c) The corresponding fluorescence intensity quantitative analysis of the images shown in (a and b). Measurements were repeated three times, and the standard deviation was plotted as error bars. (d) A schematic representation of competitive binding of folic acid and Cu/Ca-CDs. (e) The enrichment ability of Cu/Ca-CDs in L929 cells. (f) The fluorescence intensity of Cu/Ca-CDs in SCC7 cells and L929 cells at different time points (60 min and 120 min). Measurements were repeated three times, and the standard deviation was plotted as error bars. * indicates $P < 0.05$, ** indicates $P < 0.01$, *** indicates $P < 0.001$.

an additional peak at 531.1 eV appeared, which can be attributed to Cu–O/Ca-O, indicating the presence of Cu and Ca (Fig. 1k). The Cu 2p and Ca 2p spectra also validated the successful doping of copper and calcium elements (Fig. 1l and m). To further confirm this, EDS and SEM elemental mapping was performed, showing mass percentages of 6.5 % for Cu and 15.7 % for Ca (Fig. 1n and S7). The successful doping of copper and calcium, despite their large atomic radii, was attributed to the space-confined vacuum heating synthesis method. This method creates a confined reaction environment at high temperatures, effectively overcoming lattice mismatch issues. During vacuum heating, the organic precursors formed a thin-walled foam structure, confining the reactants and thereby preventing diffusion [27]. This confinement further inhibited the uncontrolled and disordered growth of the carbogenic cores during CDs formation, resulting in uniform particle sizes. Simultaneously, metal ions were passively incorporated into the CDs structure during the formation process, meaning that the metal ions do not influence the size and surface properties. To confirm this, single-doped carbon dots (Cu-CDs and Ca-CDs) were synthesized, and both exhibited similar sizes and zeta potential to the co-doped Cu/Ca-CDs (Fig. 1f, S8 and S9). Additionally, the catalytic activity of Cu/Ca-CDs was evaluated and found to be nearly identical to that of CDs without copper or calcium doping, demonstrating that copper and calcium ions were indeed incorporated into the internal structure of the Cu/Ca-CDs rather than being adsorbed on the surface (Fig. S10). This mechanism ensures the effective doping of copper and calcium while allowing stable ion retention, laying the foundation of Cu/Ca-CDs for tumor cells destruction *via* copper-induced cuproptosis and calcium overload-mediated apoptosis.

3.2. Tumor-targeting ability of Cu/Ca-CDs via binding to folate receptor

The tumor-targeting ability of Cu/Ca-CDs is a prerequisite for their effective anti-tumor efficacy [32,33]. Due to the presence of the pterin ring, which can specifically bind to the folate receptor protein on the surface of tumor cells, the as-prepared Cu/Ca-CDs are expected to exhibit tumor-targeting capability. To this end, SCC7 tumor cells, which express high levels of folate receptor, were used. As shown in Fig. 2a, SCC7 cells exhibited noticeable green fluorescence after co-incubation with Cu/Ca-CDs for 60 min. After 120 min, the fluorescence intensity increased significantly, indicating substantial cellular uptake of Cu/Ca-CDs. In contrast, when SCC7 cells were pre-incubated with folic acid, followed by the addition of Cu/Ca-CDs, minimal green fluorescence was observed at 60 min, and the fluorescence remained weak even after 120 min (Fig. 2b). The fluorescence quantification results further demonstrated that SCC7 cells incubated with Cu/Ca-CDs alone displayed much stronger fluorescence compared to those incubated with both folic acid and Cu/Ca-CDs (Fig. 2c). These findings suggest that folic acid inhibits the uptake of Cu/Ca-CDs by competing for folate receptor binding sites, confirming that Cu/Ca-CDs enter SCC7 cells by binding to folate receptor and thereby demonstrate potential for tumor-specific targeting (Fig. 2d). As a control, L929 cells, which lack folate receptor expression on their membrane surfaces, were co-incubated with Cu/Ca-CDs (Fig. 2e). After 60 min, no significant fluorescence was observed, and even after 120 min, fluorescence intensity did not increase noticeably (Fig. 2f). Although faint green fluorescence was detected in L929 cells, indicating that a small amount of Cu/Ca-CDs may have entered, this is likely due to the weakly positive zeta potential of Cu/Ca-CDs (+5 mV) (Fig. S8), which allows for slight electrostatic attraction to the negatively charged cell membrane. Consequently, these findings confirm that Cu/Ca-CDs have limited ability to enter normal cells due to the absence of folate receptor, further confirming their high specificity for tumor cells. This specificity underscores the potential of Cu/Ca-CDs for tumor-targeted therapy.

To investigate the targeting mechanism at the molecular level, molecular dynamics simulations were conducted to verify the binding of Cu/Ca-CDs to folate receptor and assess structural stability. Before the simulation, an initial model was constructed using folate receptor structure from the UniProt database (ID: P35846) with a graphene-like fragment representing the simplified Cu/Ca-CDs model. After a 120 ns simulation, an animated movie showing the interaction between folate receptor and Cu/Ca-CDs was generated from 600 trajectory frames (Movie S1). The snapshots at 0, 60, and 120 ns (Fig. 3a, b and c) indicated stable binding between Cu/Ca-CDs and folate receptor throughout the simulation. Least-squares fitting of the trajectory yielded the RMSD of atoms relative to the initial structure (Fig. 3d). The RMSD stabilized at approximately 1.5 Å after 90 ns, suggesting that the system reached equilibrium. Additionally, the number of residues in various secondary structures, including structure, β-sheets, β-bridge, bends, and α-helix, remained nearly constant during the simulation (Fig. 3e). Further analysis involved calculating the residue-wise RMSF to assess positional deviations of folate receptor amino acid residues. For comparison, a 120 ns molecular dynamics simulation of folate receptor without Cu/Ca-CDs was performed (Figs. S11 and S12 and Movie S2), and the RMSF values of the free folate receptor were used as a reference. The RMSF results showed that the binding pocket residues in the folate receptor and Cu/Ca-CDs complex exhibited significantly lower RMSF values than the free folate receptor (Fig. 3f), indicating that these residues were restrained due to interactions with Cu/Ca-CDs. Collectively, these results demonstrate that Cu/Ca-CDs target tumor cells by binding to folate receptor, facilitating their cellular uptake. This targeted delivery of Cu and Ca provides a foundation for the potential application of Cu/Ca-CDs in tumor therapy through mechanisms such as copper-induced cuproptosis and calcium overload-mediated apoptosis.

3.3. In vitro anti-tumor activity of Cu/Ca-CDs

The CCK-8 assay was used to evaluate the *in vitro* anti-tumor activity of Cu/Ca-CDs. The results demonstrated that Cu/Ca-CDs exhibited a concentration-dependent and time-dependent cytotoxic effect on tumor cells, with cell death rates increasing as the concentration and incubation time increased (Fig. 4a and S13). Specifically, when the Cu/Ca-CDs concentration reached 400 μg/mL, the viability of SCC7 tumor cells significantly decreased to approximately 30 % after 24 h of co-incubation (Fig. 4a). In contrast, as shown in Fig. S14, Cu/Ca-CDs displayed minimal toxicity toward L929 cells, with cell viability remaining approximately 80 % even at the 400 μg/mL concentration after 24 h of co-incubation. These findings not only confirm the potent cytotoxicity of Cu/Ca-CDs toward tumor cells, driven by their tumor-targeting specificity, but also demonstrate their weak toxicity to normal cells. Due to their ability to bind to the folate receptor on tumor cell membranes, Cu/Ca-CDs efficiently enter tumor cells and exert cytotoxic effects even at low concentrations. As the concentration increases, more Cu/Ca-CDs are internalized by tumor cells, thereby enhancing their therapeutic efficacy. In contrast, Cu/Ca-CDs do not specifically bind to normal cells, resulting in minimal uptake by these cells (Fig. 2e and f). Therefore, Cu/Ca-CDs exhibit weak toxicity toward normal cells, even at concentrations that effectively kill SCC7 tumor cells (400 μg/mL).

Furthermore, flow cytometry analysis was performed to confirm the therapeutic efficacy of Cu/Ca-CDs. As shown in Fig. 4b, the proportion of viable SCC7 cells decreased with increasing Cu/Ca-CDs concentration, with only 36.2 % of cells remaining viable at 400 μg/mL, consistent with the CCK-8 assay results. Additionally, both early and late apoptotic cell populations increased with higher Cu/Ca-CDs concentrations, confirming that Cu/Ca-CDs induce significant apoptosis in tumor cells. This result was further validated by propidiumiodide staining. Following treatment of SCC7 cells with increasing concentrations of Cu/Ca-CDs, the proportion of tumor cells exhibiting red fluorescence increased, indicating enhanced cell death (Fig. 4c). In all, the combined results from the CCK-8 assay, flow cytometry, and propidium iodide staining demonstrate the promising potential of Cu/Ca-CDs for tumor-targeted therapy, particularly in enhancing therapeutic selectivity and minimizing damage to normal tissues.

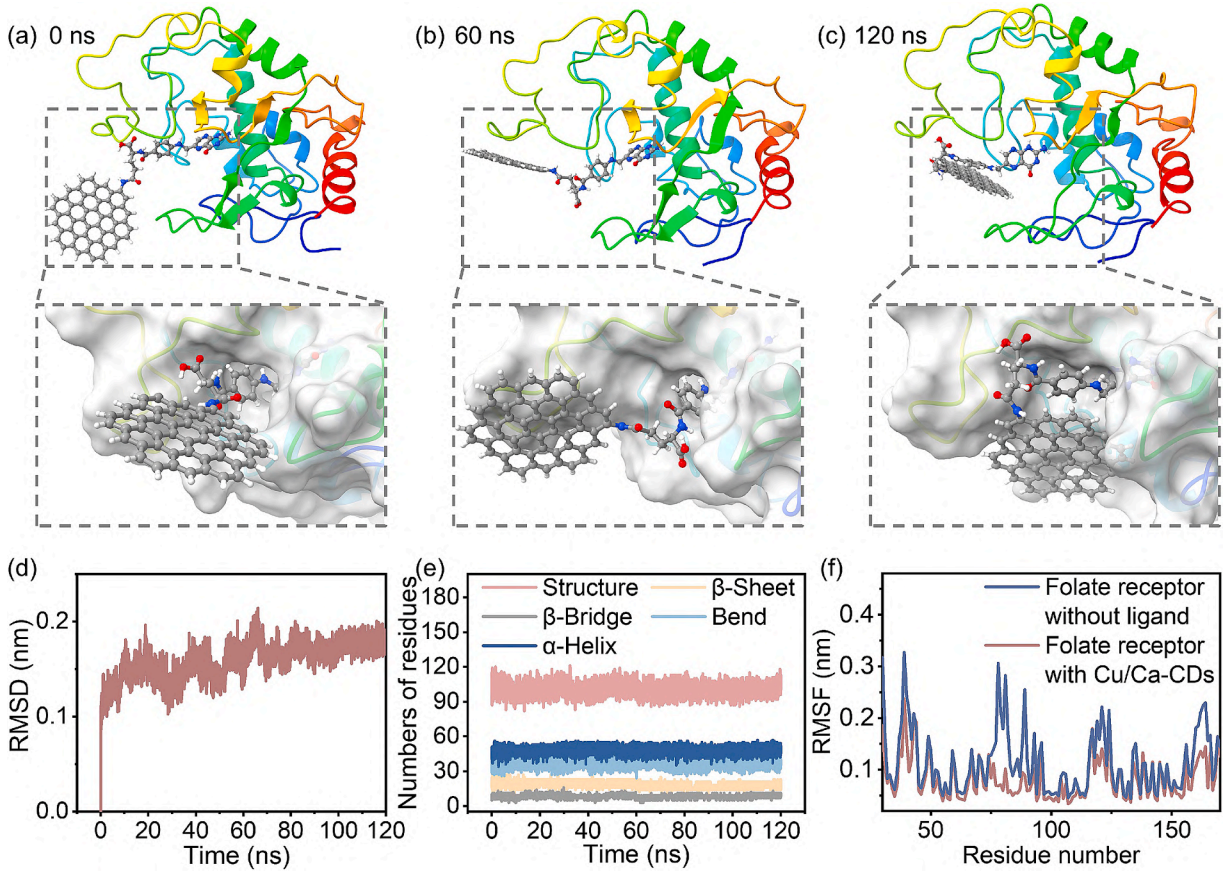

Fig. 3. (a–c) Structures of Cu/Ca-CDs binding to folate receptor, extracted from the molecular dynamics simulation trajectory at (a) 0 ns, (b) 60 ns, and (c) 120 ns, respectively. Folate receptor is depicted as a rainbow-colored cartoon and gray-shaded surface. Cu/Ca-CDs are shown in ball-and-stick mode, with carbon, hydrogen, oxygen, and nitrogen atoms colored gray, white, red, and blue, respectively. Enlarged views highlight the binding conformations of Cu/Ca-CDs within the folate receptor binding pocket at different simulation times. (d) RMSD of the Cα atoms of folate receptor in folate receptor/Cu/Ca-CDs complex against time. (e) Numbers of residues in diverse secondary structures of folate receptor. (f) RMSF values of amino acid residues 30–170 in folate receptor/Cu/Ca-CDs complex and folate receptor, respectively. (For interpretation of the references to color in this figure legend, the reader is referred to the web version of this article.)

3.4. Mechanisms of tumor cell death induced by Cu/Ca-CDs

After confirming the ability of Cu/Ca-CDs to kill tumor cells, the underlying mechanisms were explored, focusing on copper-mediated cuproptosis and calcium overload-induced apoptosis (Fig. 5a). Cuproptosis, a novel form of regulated cell death, is characterized by the oligomerization of the mitochondrial lipoylated DLAT [34–37]. To determine whether Cu/Ca-CDs induce cuproptosis, Western blot analysis was performed. As shown in Fig. 5b and Fig. S15, Cu/Ca-CDs significantly promoted DLAT oligomerization, indicating the activation of the cuproptosis pathway. Immunofluorescence staining was used to further investigate the effects of Cu/Ca-CDs on DLAT (Fig. 5c, S16 and S17). The Cu/Ca-CDs-treated group displayed markedly stronger DLAT oligomerization signals compared to the control group, further confirming the activation of the cuproptosis pathway, consistent with the Western blot results. Another hallmark of cuproptosis is the loss of Fe-S cluster proteins, including mitochondrial ferredoxin 1 (FDX1) and lipoyl synthase (LIAS), whose expression levels decrease during this process [38–41]. Western blot and qRT-PCR analyses confirmed the reduced expression of FDX1 and LIAS in the Cu/Ca-CDs-treated cells (Fig. 5d, e and S18). These results strongly support that Cu/Ca-CDs exert antitumor effects through the cuproptosis pathway.

In addition to cuproptosis, the inherent calcium in Cu/Ca-CDs is expected to synergistically enhance their anti-tumor activity through calcium ions overload [42]. To verify Ca^{2+} overload-induced apoptosis, Rhod-2 calcium probes were used to monitor changes in intracellular Ca^{2+} levels in SCC7 tumor cells after incubation with Cu/Ca-CDs. As shown in Fig. 5f, red fluorescence intensity increased over time, indicating a progressive release of Ca^{2+} from Cu/Ca-CDs into the tumor cells. Excessive intracellular Ca^{2+} disrupts mitochondrial function, thereby activating the mitochondria-mediated apoptosis pathway and inducing tumor cell death [43,44]. To investigate the apoptosis mechanism induced by Ca^{2+} overload, the expression levels of key apoptosis-related proteins, including the pro-apoptotic proteins Bax, Caspase 9, and Caspase 3, as well as the anti-apoptotic protein Bcl-2, were analyzed. Fig. 5g and S19 show that Cu/Ca-CDs treatment significantly upregulated Bax, Caspase 9, and Caspase 3, while Bcl-2 was downregulated. These changes indicate that Cu/Ca-CDs deliver calcium ions specifically to tumor cells, causing calcium overload and activating the mitochondria-mediated apoptosis pathway.

Since both cuproptosis and calcium overload-induced apoptosis affect mitochondria, the impact of Cu/Ca-CDs on mitochondrial dysfunction was investigated by measuring the mitochondrial membrane potential (ΔΨm) using JC-1 dye staining. Healthy mitochondria with high ΔΨm emit red fluorescence, while damaged mitochondria with low ΔΨm emit green fluorescence (Fig. 5h) [45]. The Cu/Ca-CDs-treated group showed strong green fluorescence and weak red fluorescence, similar to the positive control treated with the mitochondrial electron transport chain inhibitor CCCP (Fig. 5i). Further quantitative fluorescence analysis revealed that the red/green ratio in the Cu/Ca-CDs-treated group was only one-sixteenth of that in the control group (Fig. S20). These results indicate significant mitochondrial membrane depolarization and severe mitochondrial damage [46]. All above findings demonstrate that Cu/Ca-CDs function as targeted carriers for

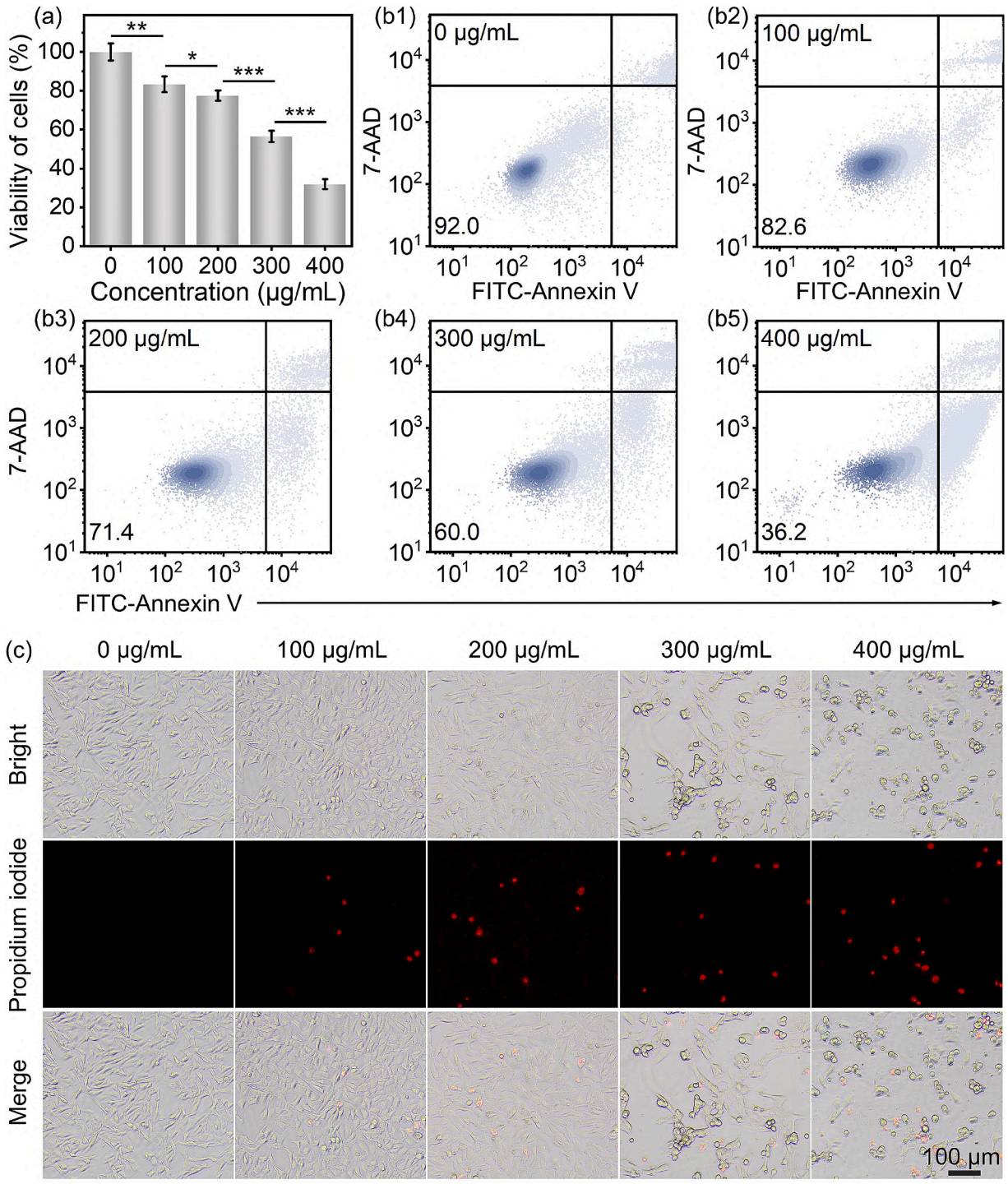

Fig. 4. *In vitro* anti-tumor activity of Cu/Ca-CDs. (a) Cell viability of SCC7 cells after 24 h treatment of Cu/Ca-CDs at different concentrations (0, 100, 200, 300, and 400 μg/mL). Measurements were repeated three times, and the standard deviation was plotted as error bars. * indicates $P < 0.05$, ** indicates $P < 0.01$, *** indicates $P < 0.001$. (b) Flow cytometry analysis of apoptosis in SCC7 cells which are treated with different concentrations of Cu/Ca-CDs (0, 100, 200, 300, and 400 μg/mL). (c) Propidium iodide staining images of SCC7 cells at different concentrations (red for dead cells). (For interpretation of the references to color in this figure legend, the reader is referred to the web version of this article.)

copper and calcium ions, creating an environment of copper and calcium overload within tumor cells. Through the synergistic mechanisms of cuproptosis and calcium overload-induced apoptosis, Cu/Ca-CDs disrupt mitochondrial function and ultimately induce tumor cell death. These results highlight the significant potential of Cu/Ca-CDs for tumor therapy.

3.5. *In vivo dual-mode imaging of Cu/Ca-CDs*

In clinical treatment, accurately determining the distribution and concentration of therapeutic agents within tumor tissues is crucial for minimizing damage to normal tissues and reducing side effects, which remains a significant challenge for traditional drugs [47,48]. To address this issue, Cu/Ca-CDs offer a promising solution due to their unique fluorescence properties and the CT imaging capabilities conferred by the

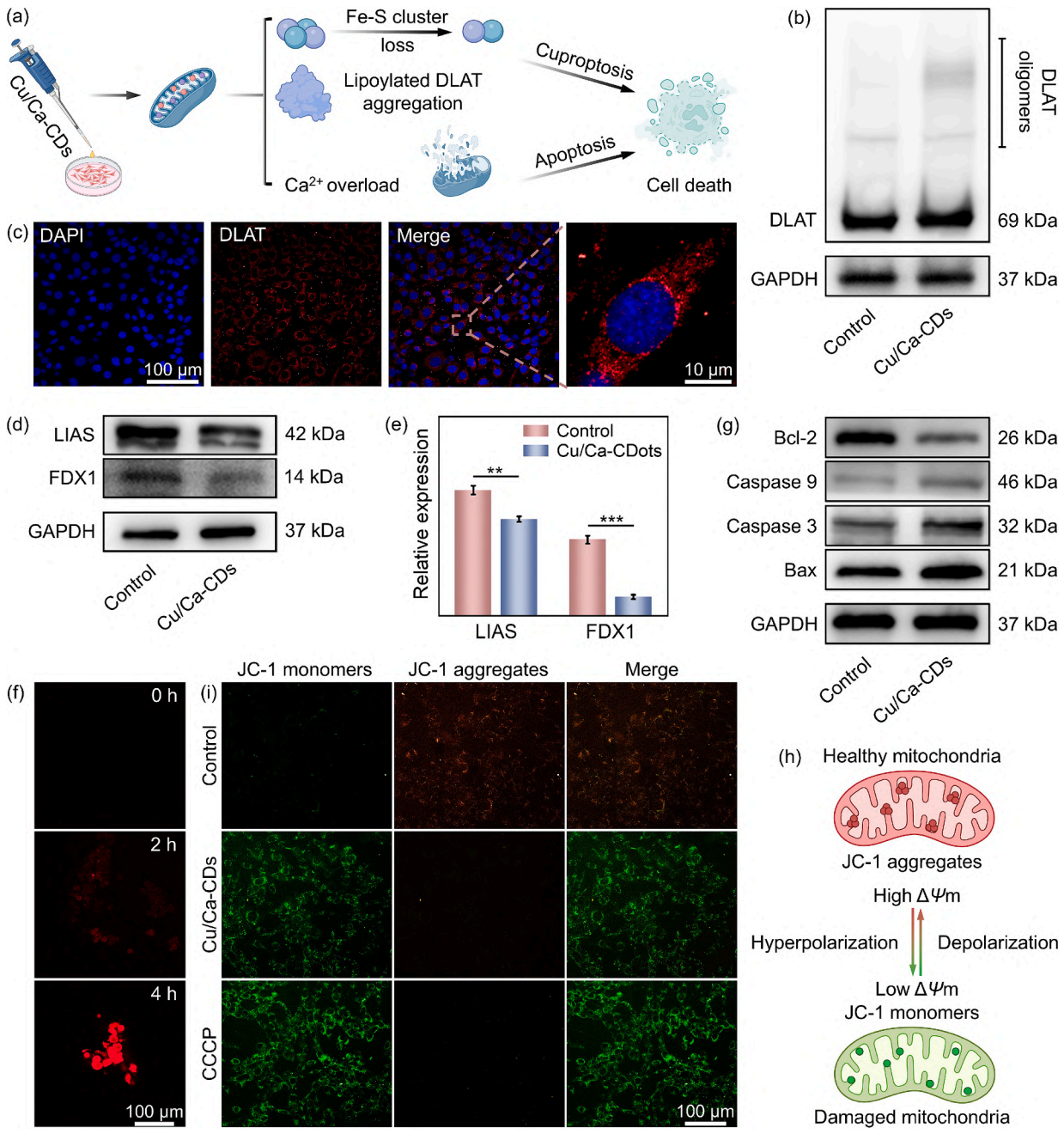

Fig. 5. *In vitro* evaluation of cuproptosis and apoptosis induced by Cu/Ca-CDs. (a) Schematic illustration of Cu/Ca-CDs-induced cuproptosis and apoptosis. (b) Western blot analysis of the protein expressions of DLAT. (c) Immunofluorescence images of SCC7 cells co-cultured with Cu/Ca-CDs stained with anti-DLAT antibody (red) and DAPI (blue). (d) Western blot analysis of the protein expressions of LIAS and FDX1 after different treatments. (e) Capability of Cu/Ca-CDs to suppress FDX1 and LIAS expression *via* RT-qPCR. Measurements were repeated three times, and the standard deviation was plotted as error bars. * indicates $P < 0.05$, ** indicates $P < 0.01$, *** indicates $P < 0.001$. (f) CLSM images of Ca^{2+} levels in the mitochondria of SCC7 cells as detected by Rhod-2 at different time points. (g) Western blot analysis of the protein expressions of Bcl-2, Caspase 9, Caspase 3 and Bax. (h) Schematic illustration of the fluorescent indicator JC-1 dye which was applied for the detection of mitochondrial membrane potential (ΔΨm). (i) CLSM images of JC-1-stained SCC7 cells. (For interpretation of the references to color in this figure legend, the reader is referred to the web version of this article.)

doped high atomic number elements, copper and calcium. Based on the excellent fluorescence properties of Cu/Ca-CDs, their *in vivo* fluorescence imaging was investigated (Fig. 6a). As shown in Fig. 6b, the Cu/Ca-CDs-treated group exhibited a significant fluorescence signal, clearly delineating the tumor. Furthermore, the fluorescence intensity of Cu/Ca-CDs within the tumor remained stable over time, with the tumor location still detectable 60 min post-injection (Fig. 6c). This indicates strong imaging capability and effective accumulation within the tumor, laying a foundation for their *in vivo* anti-tumor efficacy. In addition, the incorporation of copper and calcium enhances the X-ray absorption capacity of Cu/Ca-CDs, enabling their use as a CT contrast agent. Fig. 6d shows that the CT signal intensity increased with higher Cu/Ca-CDs concentrations, establishing a linear relationship between concentration and signal strength. This provides an effective method for quantifying Cu/Ca-CDs accumulation in tumors *via* CT imaging and supports drug monitoring and precise dosing. The CT imaging performance of Cu/Ca-CDs was further evaluated *in vivo* (Fig. 6e and f). Compared to the control group, Cu/Ca-CDs clearly delineated the tumor boundaries,

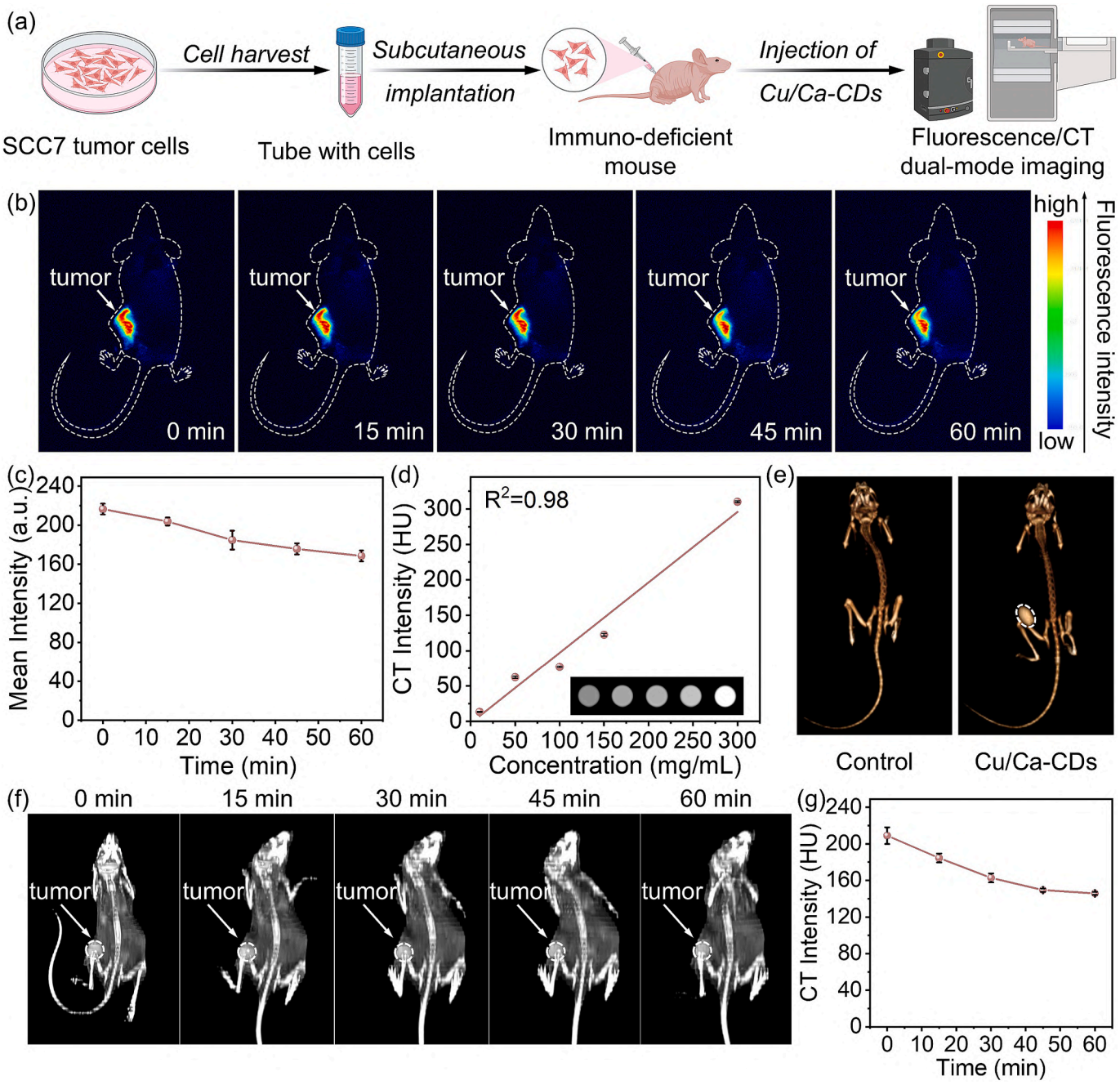

Fig. 6. *In vivo* dual-mode imaging of Cu/Ca-CDs. (a) Experimental design for dual-mode imaging. (b) The fluorescence imaging capabilities of Cu/Ca-CDs at different times (0, 15, 30, 45 and 60 min). (c) Quantitative evaluation based on the fluorescence imaging data for Cu/Ca-CDs. Measurements were repeated three times, and the standard deviation was plotted as error bars. (d) CT intensity of Cu/Ca-CDs across varying concentrations. Measurements were repeated three times, and the standard deviation was plotted as error bars. (e) *In vivo* 3D CT images of tumor-bearing mice without (left) and with (right) intratumor injection of Cu/Ca-CDs. (f) CT imaging capabilities of Cu/Ca-CDs at different times (0, 15, 30, 45, and 60 min). The white dashed box in each panel highlights the location of the tumor. (g) Trend analysis of CT intensity over time following the administration of Cu/Ca-CDs. Measurements were repeated three times, and the standard deviation was plotted as error bars.

demonstrating their advantage in tumor CT imaging. Moreover, the sustained CT signal confirms the accumulation of Cu/Ca-CDs in the tumor (Fig. 6f and g), consistent with the fluorescence imaging results. Taken together, the exceptional fluorescence and CT imaging capabilities of Cu/Ca-CDs enable dual-mode imaging, allowing real-time tracking of their distribution and concentration within tumors. This facilitates precise and controlled drug delivery, optimizing dosing regimen based on imaging feedback, and ultimately enhancing therapeutic outcomes.

3.6. *In vivo anti-tumor efficacy of Cu/Ca-CDs*

As shown in Fig. 7a, a subcutaneous SCC7 tumor model was established to investigate the *in vivo* anti-tumor effects of Cu/Ca-CDs administered *via* tail vein injection. To confirm the feasibility of this administration route, a hemolysis assay was performed to evaluate the blood compatibility of Cu/Ca-CDs. The results indicated that the hemolysis rate of Cu/Ca-CDs was below the 5 % threshold (Fig. 7b), demonstrating good blood compatibility. During the subsequent treatment, the tumor volume in the Cu/Ca-CDs group gradually decreased

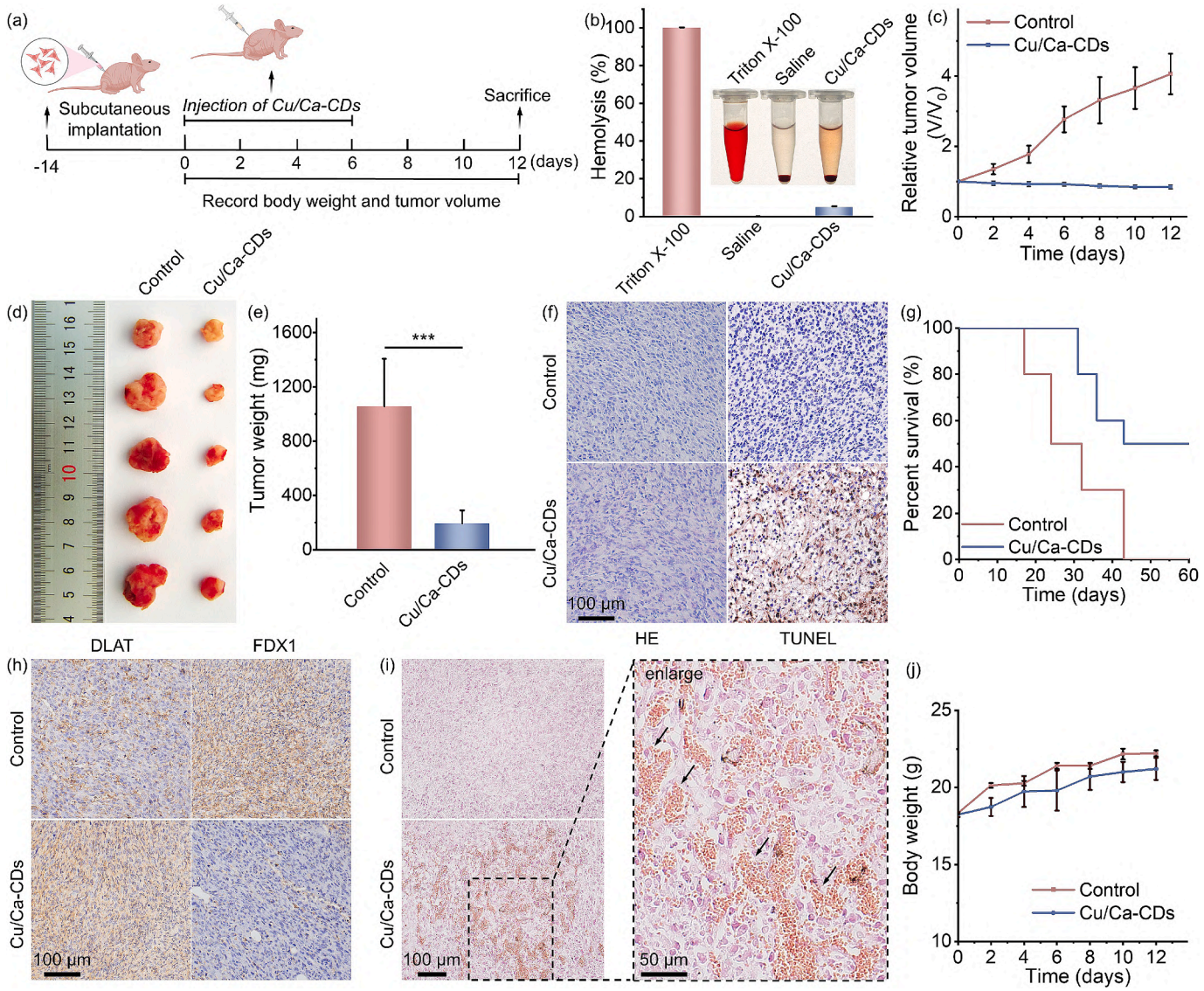

Fig. 7. *In vivo* anti-tumor efficacy of Cu/Ca-CDs. (a) Schematic of the experimental protocol *in vivo*. (b) Hemolysis tests of Cu/Ca-CDs. (c) Tumor growth trajectories in SCC7 tumor-bearing mice post-Cu/Ca-CDs treatment. Tumor progression was monitored over a 12-day period. Measurements were repeated three times, and the standard deviation was plotted as error bars. (d) Photographs of excised tumor after treated with PBS and Cu/Ca-CDs *via* intratumor injection. (e) Weights of the extracted tumors. Measurements were repeated three times, and the standard deviation was plotted as error bars. (f) H&E and TUNEL staining of tumor tissues from the different treatment groups. (g) Survival tracking of tumor-bearing mice over the course of the 60-day treatment in each group. (h) Immunohistochemical staining images of tumor sections showing DLAT and FDX1 expression. (i) Alizarin Red staining of the tumor tissues. (j) Body weight fluctuations of SCC7 tumor-bearing mice over the 12-day treatment span. Measurements were repeated three times, and the standard deviation was plotted as error bars. (For interpretation of the references to color in this figure legend, the reader is referred to the web version of this article.)

(Fig. 7c). After 12 days of treatment, significant tumor ablation was observed in the Cu/Ca-CDs group (Fig. 7d). Quantitative analysis showed that the tumor weight in the Cu/Ca-CDs group was only one-fifth that of the PBS-treated control group (Fig. 7e), confirming the excellent anti-tumor efficacy of Cu/Ca-CDs. Furthermore, H&E staining and TUNEL staining were conducted to assess cellular changes within the tumor tissue (Fig. 7f). The results revealed extensive damage to tumor cells in the Cu/Ca-CDs group, indicating effective anti-tumor activity of Cu/Ca-CDs. Consequently, the Cu/Ca-CDs group exhibited higher survival rates over a 60-day observation period, as shown by the survival curve (Fig. 7g).

Subsequently, the *in vivo* anti-tumor mechanism of Cu/Ca-CDs was explored. Immunohistochemical staining of DLAT and FDX1 in tumor tissues was performed to verify the activation of the cuproptosis pathway. As shown in Fig. 7h, DLAT expression levels increased while FDX1 expression decreased in the Cu/Ca-CDs group compared to the control group, which were consistent with the *in vitro* Western blot findings, confirming the activation of the cuproptosis pathway. To verify calcium accumulation in tumor tissues, Alizarin Red S staining was conducted, as this dye binds to Ca^{2+} and forms red precipitates. Fig. 7i shows a significantly higher level of red staining in the Cu/Ca-CDs group compared to the control group, indicating the activation of calcium overload-mediated apoptosis.

Importantly, no significant changes in body weight were observed in the Cu/Ca-CDs group throughout the treatment period (Fig. 7j), demonstrating the excellent biosafety of Cu/Ca-CDs. Additionally, the timely excretion of therapeutic agents from the body is crucial for ensuring their safety. To investigate the excretion of Cu/Ca-CDs, we employed ICP-MS to measure the concentrations of copper and calcium ions in tumor tissue, heart, liver, spleen, lung, kidney, feces, and urine from both the control group (PBS injection) and the Cu/Ca-CDs-treated group at various time points (0, 6, 12, 24, and 48 h) (Fig. S21). The ICP-

MS results revealed that after circulating in the bloodstream for a period of time, copper and calcium ions were detected in tumor tissues at approximately 6 h, with their concentration continuing to rise until 12 h, indicating progressive accumulation in the tumor. Over time, the levels of copper and calcium in the tumor gradually decreased, suggesting the gradual metabolism of Cu/Ca-CDs within the tumor. During the entire circulation process, no significant increase in copper or calcium levels was observed in the heart, spleen, or lung. However, in the kidney and liver, the concentrations of copper and calcium gradually rose until reaching their peak at 6 h, after which they gradually declined. Furthermore, copper and calcium ions were detected in both feces and urine, indicating that Cu/Ca-CDs are primarily metabolized by the kidney and liver, rather than by the heart, spleen, or lung. The efficient clearance of copper and calcium ions further ensures that major organs are not exposed to potential side effects from Cu/Ca-CDs. H&E staining of the heart, liver, spleen, lungs, and kidneys was further performed and showed no pathological damage or inflammation in the Cu/Ca-CDs-treated group compared to the control group, confirming the safety of Cu/Ca-CDs for *in vivo* applications (Fig. S22). These results collectively demonstrate that Cu/Ca-CDs, administered *via* tail vein injection, effectively target tumor tissues. Once internalized by tumor cells, Cu/Ca-CDs release the doped copper and calcium, inducing cell death through copper-induced cuproptosis and calcium overload-mediated apoptosis. This targeted tumor-killing mechanism, combined with minimal damage to normal tissues due to efficient clearance of copper and calcium ions, highlights the significant clinical potential of Cu/Ca-CDs for tumor therapy.

4. Conclusions

Metal ion-regulated tumor therapy has emerged as a novel approach in cancer treatment [49]. However, its clinical application remains limited due to the lack of tumor-targeting specificity [50]. In this study, copper and calcium co-doped carbon dots (Cu/Ca-CDs) were successfully synthesized using a space-confined vacuum heating method, demonstrating excellent tumor-targeting ability and significant anti-tumor efficacy. Characterization analyses confirmed the successful incorporation of copper and calcium into the Cu/Ca-CDs, which possess a pterin ring structure that facilitates specific binding to folate receptor on tumor cells. This targeted mechanism enabled the selective uptake of Cu/Ca-CDs by tumor cells while sparing normal cells, thereby enhancing therapeutic selectivity. After uptake by tumor cells, copper-induced cuproptosis and calcium overload-mediated apoptosis synergistically induced tumor cell death. The *in vivo* dual-mode imaging capability of Cu/Ca-CDs, enabled by their fluorescence and computed tomography (CT) imaging properties, allowed real-time tracking of their distribution and accumulation within tumors. This imaging-guided approach confirmed the effective delivery of Cu/Ca-CDs to tumor tissues and minimized the risk of damage to normal tissues. *In vivo* studies further demonstrated the potent anti-tumor effects of Cu/Ca-CDs, showing significant tumor volume reduction and increased survival rates in tumor-bearing mice. Importantly, no significant toxicity to normal tissues or changes in body weight were observed, underscoring the biosafety of Cu/Ca-CDs. In conclusion, nanoparticle-mediated metal ion delivery has been widely explored for tumor diagnosis and therapy. However, the development and clinical translation of metal-ion-doped nanomaterials with tumor-targeting functionality remain challenging. The Cu/Ca-CDs synthesized in this study exhibit significant potential for tumor-targeted therapy, paving the way for the development of more effective and safer cancer treatments and offering a viable strategy for precision oncology.

CRediT authorship contribution statement

Wenqian Zheng: Writing – review & editing, Writing – original draft, Visualization, Validation, Supervision, Software, Resources, Project administration, Methodology, Funding acquisition, Formal analysis, Data curation, Conceptualization. **Yang Liu:** Visualization, Validation, Software, Methodology, Formal analysis, Data curation. **Jinru Liu:** Visualization, Methodology, Investigation, Formal analysis, Data curation. **Yuping Zhao:** Visualization, Validation, Methodology, Formal analysis, Data curation. **Peiyu Wang:** Methodology, Investigation. **Yi Wang:** Writing – review & editing, Visualization. **Yuxuan Wang:** Resources, Investigation. **Zeyu Lu:** Methodology, Formal analysis. **Xiaofan Liu:** Investigation, Formal analysis. **Yaru Shi:** Investigation, Formal analysis. **Na Zhou:** Writing – review & editing, Visualization. **Fermín Eduardo González:** Writing – review & editing, Visualization. **Hongchen Sun:** Writing – review & editing, Supervision, Resources, Project administration, Conceptualization. **Ding Zhou:** Writing – review & editing, Writing – original draft, Validation, Software, Resources, Project administration, Funding acquisition, Conceptualization. **Xiaowei Xu:** Writing – review & editing, Validation, Supervision, Resources, Project administration, Funding acquisition, Conceptualization.

Declaration of competing interest

The authors declare that they have no known competing financial interests or personal relationships that could have appeared to influence the work reported in this paper.

Acknowledgements

This work was supported by grants from the National Key Research and Development Program for Young Scientists (2022YFA1105800), the National Natural Science Foundation of China (82470957), Jilin Province Science and Technology Research (Project No. YDZJ202501-ZYTS020), the Bethune Plan Project of Jilin University (2024B14), and Graduate Innovation Fund of Jilin University (2024CX262).

Appendix A. Supplementary data

Supplementary data to this article can be found online at https://doi.org/10.1016/j.jcis.2025.137337.

Data availability

Data will be made available on request.

References

[1] A. Psyrri, J. Fayette, K. Harrington, M. Gillison, M.J. Ahn, S. Takahashi, J. Weiss, J. P. Machiels, S. Baxi, A. Vasilyev, A. Karpenko, M. Dvorkin, C.Y. Hsieh, S. C. Thungappa, P.P. Segura, I. Vynnychenko, R. Haddad, S. Kasper, P.S. Mauz, V. Baker, P. He, B. Evans, S. Wildsmith, R.F. Olsson, A. Yovine, J.F. Kurland, N. Morsli, T.Y. Seiwert, Durvalumab with or without tremelimumab versus the EXTREME regimen as first-line treatment for recurrent or metastatic squamous cell carcinoma of the head and neck: KESTREL, a randomized, open-label, phase III study, Ann. Oncol. 34 (3) (2023) 262–274.

[2] N. Singh, S. Temin, S. Baker, E. Blanchard, J.R. Brahmer, P. Celano, N. Duma, P. M. Ellis, I.B. Elkins, R.Y. Haddad, P.J. Hesketh, D. Jain, D.H. Johnson, N.B. Leighl, H. Mamdani, G. Masters, P.R. Moffitt, T. Phillips, G.J. Riely, A.G. Robinson, R. Rosell, J.H. Schiller, B.J. Schneider, D.R. Spigel, I.A. Jaiyesimi, Therapy for stage IV non-small-cell lung cancer without driver alterations: ASCO living guideline, J. Clin. Oncol. 40 (28) (2022) 3323–3343.

[3] Y. Doki, J.A. Ajani, K. Kato, J. Xu, L. Wyrwicz, S. Motoyama, T. Ogata, H. Kawakami, C.-H. Hsu, A. Adenis, F. El Hajbi, M. Di Bartolomeo, M.I. Braghiroli, E. Holtved, S.A. Ostoich, H.R. Kim, M. Ueno, W. Mansoor, W.-C. Yang, T. Liu, J. Bridgewater, T. Makino, I. Xynos, X. Liu, M. Lei, K. Kondo, A. Patel, J. Gricar, I. Chau, Y. Kitagawa, Nivolumab combination therapy in advanced esophageal squamous-cell carcinoma, N. Engl. J. Med. 386 (5) (2022) 449–462.

[4] M.C.G. Winge, L.N. Kellman, K. Guo, J.Y. Tang, S.M. Swetter, S.Z. Aasi, K.Y. Sarin, A.L.S. Chang, P.A. Khavari, Advances in cutaneous squamous cell carcinoma, Nat. Rev. Cancer 23 (7) (2023) 430–449.

[5] H. Sung, J. Ferlay, R.L. Siegel, M. Laversanne, I. Soerjomataram, A. Jemal, F. Bray, Global cancer statistics 2020: GLOBOCAN estimates of incidence and mortality worldwide for 36 cancers in 185 countries, Ca-Cancer J. Clin. 71 (3) (2021) 209–249.

[6] S.J. Peng, F.F. Xiao, M.W. Chen, H.L. Gao, Tumor-microenvironment-responsive nanomedicine for enhanced cancer immunotherapy, Adv. Sci. 9 (1) (2021) 2103836.

[7] L.M. Song, Q.F. Zhao, S.P. Feng, Y. He, Y. Li, S.L. Wang, J.H. Zhang, Depolymerizable enzymatic cascade nanoreactor for self-enhancing targeting synergistic tumor therapy, Adv. Funct. Mater. 34 (9) (2024) 2414121.

[8] M.J. Cui, B. Xu, L.H. Wang, Recent advances in multi-metallic-based nanozymes for enhanced catalytic cancer therapy, Bmemat 2 (1) (2023) 12043.

[9] M.Y. Chen, C. Xu, C.H. Wang, N. Huang, Z.X. Bian, Y.X. Xiao, J. Ruan, F.Y. Sun, S. Shi, Three birds with one stone: Copper ions assisted synergistic cuproptosis/chemodynamic/photothermal therapy by a three-pronged approach, Adv. Healthc. Mater. 13 (29) (2024) 2401567.

[10] C.E. Du, X. Guo, X. Qiu, W.X. Jiang, X.T. Wang, H.J. An, J.X. Wang, Y.L. Luo, Q. Y. Du, R.Y. Wang, C. Cheng, Y. Guo, H. Teng, H.T. Ran, Z.G. Wang, P. Li, Z.Y. Zhou, J.L. Ren, Self-reinforced bimetallic mito-jammer for Ca^{2+} overload-mediated cascade mitochondrial damage for cancer cuproptosis sensitization, Adv. Sci. 11 (15) (2024) 2306031.

[11] G.H. Hou, Y.D. Chen, H.L. Lei, Y.J. Lu, L. Liu, Z.H. Han, S.M. Sun, J.R. Li, L. Cheng, Bimetallic peroxide nanoparticles induce PANoptosis by disrupting ion homeostasis for enhanced immunotherapy, Sci. Adv. 10 (45) (2024) eadp7160.

[12] P. Tsvetkov, S. Coy, B. Petrova, M. Dreishpoon, A. Verma, M. Abdusamad, J. Rossen, L. Joesch-Cohen, R. Humeidi, R.D. Spangler, J.K. Eaton, E. Frenkel, M. Kocak, S.M. Corsello, S. Lutsenko, N. Kanarek, S. Santagata, T.R. Golub, Copper induces cell death by targeting lipoylated TCA cycle proteins, Science 375 (6586) (2022) 1254–1261.

[13] Q.X. Huang, J.L. Liang, Q.W. Chen, X.K. Jin, M.T. Niu, C.Y. Dong, X.Z. Zhang, Metal-organic framework nanoagent induces cuproptosis for effective immunotherapy of malignant glioblastoma, Nano Today 51 (2023) 101911.

[14] J. Zhou, Q. Yu, J. Song, S. Li, X.L. Li, B. Kang, H.Y. Chen, J.J. Xu, Photothermally triggered copper payload release for cuproptosis-promoted cancer synergistic therapy, Angew. Chem. Int. Ed. 62 (12) (2023) e202213922.

[15] T.T. Liu, Z.H. Zhou, M.X. Zhang, P.X. Lang, J. Li, Z.M. Liu, Z.R. Zhang, L. Li, L. Zhang, Cuproptosis-immunotherapy using PD-1 overexpressing T cell membrane-coated nanosheets efficiently treats tumor, J. Control. Release 362 (2023) 502–512.

[16] Z. Yang, Z. Zhao, H.L. Cheng, Y.H. Shen, A.J. Xie, M.Z. Zhu, In-situ fabrication of novel Au nanoclusters-Cu^{2+}@sodium alginate/hyaluronic acid nanohybrid gels for cuproptosis enhanced photothermal/photodynamic/chemodynamic therapy *via* tumor microenvironment regulation, J. Colloid Interface Sci. 641 (2023) 215–228.

[17] S. Bai, Y.L. Lan, S.Y. Fu, H.W. Cheng, Z.X. Lu, G. Liu, Connecting calcium-based nanomaterials and cancer: From diagnosis to therapy, Nano-Micro Lett. 14 (1) (2022) 00894.

[18] Z.M. Liu, N. Zeng, J. Yu, C.Y. Huang, Q.Q. Huang, A novel dual MoS_2/FeGA quantum dots endowed injectable hydrogel for efficient photothermal and boosting chemodynamic therapy, NanoBiotechnology 10 (2022) 998571.

[19] X. Yuan, Y. Kang, J.R. Dong, R.Y. Li, J.M. Ye, Y.Y. Fan, J.W. Han, J.H. Yu, G.J. Ni, X.Y. Ji, D. Ming, Self-triggered thermoelectric nanoheterojunction for cancer catalytic and immunotherapy, Nat. Commun. 14 (1) (2023) 40954.

[20] Z.H. Guo, X.H. Gao, J.S. Lu, Y. Li, Z.P. Jin, A. Fahad, N.U. Pambe, H. Ejima, X. D. Sun, X.M. Wang, W.S. Xie, G.F. Zhang, L.Y. Zhao, Apoptosis and paraptosis induced by disulfiram-loaded Ca^{2+}/Cu^{2+} dual-ions nano trap for breast cancer treatment, ACS Nano 18 (9) (2024) 6975–6989.

[21] X.M. Zhang, L.Y. Li, B.Z. Wang, Z.P. Cai, B.H. Zhang, F. Chen, G.C. Xing, K. Li, S. N. Qu, Donor-acceptor type supra-carbon-dots with long lifetime photogenerated radicals boosting tumor photodynamic therapy, Angew. Chem. Int. Ed. 63 (49) (2024) e202410522.

[22] J.X. Dong, G.X. Liu, Y.V. Petrov, Y.J. Feng, D.C. Jia, V.E. Baulin, A.Y. Tsivadze, Y. Zhou, B.Q. Li, EDTA-functionalized carbon dots-metal nanozymes based on coordination chemistry: Species of metal ions determines enzyme-mimicking catalyzed activities, ACS Mater. Lett. 6 (4) (2024) 1112–1119.

[23] S.W. Zhou, H.J. Cai, Z.Y. Tang, S.Y. Lu, Carbon dots encapsulated zeolitic imidazolate framework-8 as an enhanced multi-antioxidant for efficient cytoprotection to HK-2 cells, J. Colloid Interface Sci. 676 (2024) 726–738.

[24] P. Chen, X. He, Y. Hu, X.L. Tian, X.Q. Yu, J. Zhang, Spleen-targeted mRNA delivery by amphiphilic carbon dots for tumor immunotherapy, ACS Appl. Mater. Interfaces 15 (16) (2023) 19937–19950.

[25] C. Chen, J.Y. Ke, X.E. Zhou, W. Yi, J.S. Brunzelle, J. Li, Eu-Leong Yong, H. EricXu, Karsten Melcher, Structural basis for molecular recognition of folic acid by folate receptors, Nature 500 (7463) (2013) 486–489.

[26] M. Scaranti, E. Cojocaru, S. Banerjee, U. Banerji, Exploiting the folate receptor α in oncology, Nat. Rev. Clin. Oncol. 17 (6) (2020) 349–359.

[27] D. Zhou, P.T. Jing, Y. Wang, Y.C. Zhai, D. Li, Y. Xiong, A.V. Baranov, S.N. Qu, A. L. Rogach, Carbon dots produced *via* space-confined vacuum heating: Maintaining efficient luminescence in both dispersed and aggregated states, Nanoscale Horiz. 4 (2) (2019) 388–395.

[28] F. Mocci, L. de Villiers Engelbrecht, C. Olla, A. Cappai, M.F. Casula, C. Melis, L. Stagi, A. Laaksonen, C.M. Carbonaro, Carbon nanodots from an in silico perspective, Chem. Rev. 122 (16) (2022) 13709–13799.

[29] J.Z. Guo, Y.F. Chen, P. Zhang, G. Li, X.N. Yang, C.F. Wang, S. Chen, Easy-to-perform organic-solvent-free synthesis of carbon dots with strong green photoluminescence, Chin. Chem. Lett. 35 (3) (2024) 108481.

[30] J.Y. Chen, F. Li, J. Gu, X. Zhang, M. Bartoli, J.B. Domena, Y.Q. Zhou, W. Zhang, V. Paulino, B.C.L.B. Ferreira, N.M. Brejcha, L. Luo, C. Arduino, F. Verde, F. L. Zhang, F.W. Zhang, A. Tagliaferro, J.-H. Olivier, Y.B. Zhang, R.M. Leblanc, Cancer cells inhibition by cationic carbon dots targeting the cellular nucleus, J. Colloid Interface Sci. 637 (2023) 193–206.

[31] F. Zhao, H.Y. Yu, L.Y. Liang, C. Wang, D.E. Shi, X.Y. Zhang, Y. Ying, W. Cai, W. C. Li, J. Li, J.W. Zheng, L. Qiao, S.L. Che, J. Yu, Redox homeostasis disruptors based on metal-phenolic network nanoparticles for chemo/chemodynamic synergistic tumor therapy through activating apoptosis and cuproptosis, Adv. Healthc. Mater. 12 (29) (2023) 2301346.

[32] Y.H. He, M.N. Wang, X.L. Li, T. Yu, X. Gao, Targeted MIP-3β plasmid nanoparticles induce dendritic cell maturation and inhibit M2 macrophage polarisation to suppress cancer growth, Biomaterials 249 (2020) 120046.

[33] Y.T. Wen, H.Z. Bai, J.L. Zhu, X. Song, G.P. Tang, J. Li, A supramolecular platform for controlling and optimizing molecular architectures of siRNA targeted delivery vehicles, Sci. Adv. 6 (31) (2020) eabc2148.

[34] Z. Li, L. Cheng, X. Xu, R. Jia, S.Y. Zhu, Q. Zhang, G.T. Cheng, B.Q. Wu, Z.L. Liu, X. L. Tong, B. Xiao, F.Y. Dai, Cuproptosis-based layer-by-layer silk fibroin nanoplatform-loaded PD-L1 siRNA combining photothermal and chemodynamic therapy against metastatic breast cancer, Mater. Today Bio 29 (2024) 101298.

[35] Y. Liu, R. Niu, H. Zhao, Y.H. Wang, S.Y. Song, H.J. Zhang, Y.L. Zhao, Single-site nanozymes with a highly conjugated coordination structure for antitumor immunotherapy *via* cuproptosis and cascade-enhanced T lymphocyte activity, J. Am. Chem. Soc. 146 (6) (2024) 3675–3688.

[36] L.H. Qiao, W.T. Xuan, Y.J. Ou, L. Li, S.Z. Wu, Y.X. Guo, M. Liu, D.S. Yu, Q.H. Chen, J.M. Yuan, M.X. Zuo, C.Q. Wei, O.C. Yi, H.W. Li, D. Cheng, Z.Q. Yu, Z.J. Li, Tumor microenvironment activation amplify oxidative stress promoting tumor energy remodeling for mild photothermal therapy and cuproptosis, Redox Biol. 75 (2024) 103260.

[37] C.Z. Yan, H.Y. Lv, Y.F. Feng, Y.H. Li, Z.X. Zhao, Inhalable nanoparticles with enhanced cuproptosis and cGAS-STING activation for synergistic lung metastasis immunotherapy, Acta Pharm. Sin. B 14 (8) (2024) 3697–3710.

[38] N. Wang, Y.C. Liu, D.Z. Peng, Q.Y. Zhang, Z.B. Zhang, L.N. Xu, L.H. Yin, X.R. Zhao, Z. Lu, J.Y. Peng, Copper-based composites nanoparticles improve triple-negative breast cancer treatment with induction of apoptosis-cuproptosis and immune activation, Adv. Healthc. Mater. 13 (28) (2024) 2401646.

[39] W.J. Xu, A.L. Suo, A.J.M. Aldai, Y.P. Wang, J.J. Fan, Y.X. Xia, J.X. Xu, Z.X. Chen, H. C. Zhao, M.Z. Zhang, J.M. Qian, Hollow calcium/copper bimetallic amplifier for cuproptosis/paraptosis/apoptosis cancer therapy *via* cascade reinforcement of endoplasmic reticulum stress and mitochondrial dysfunction, ACS Nano 18 (43) (2024) 30053–30068.

[40] K.R. Chen, A.W. Zhou, X.Y. Zhou, J.L. He, Y.R. Xu, X.H. Ning, Cellular Trojan Horse initiates bimetallic Fe-Cu MOF-mediated synergistic cuproptosis and ferroptosis against malignancies, Sci. Adv. 10 (15) (2024) eadk3201.

[41] F. Zhao, H.Y. Yu, C. Wang, J.C. Xu, H. Gao, Y. Ying, W.C. Li, J. Li, J.W. Zheng, L. Qiao, S.L. Che, J. Yu, Copper/iron bimetal phenolic networks boosted apoptosis/ferroptosis/cuproptosis combined tumor therapy through dual glutathione depletion, Chem. Eng. J. 500 (2024) 157408.

[42] J.H. Yan, H.Y. Chen, C.F. Guimarães, R.L. Reis, Z.H. Zhu, T.Y. Wang, F.L. Zhang, Y. Q. Lv, Q.H. Zhou, X.Y. Kong, J.S. Shi, Cu^{+}/Ca^{2+} dual-overload strategy assisted by metabolic-symbiotic-destruction for tumor apoptosis and tumor immune activation, Adv. Funct. Mater. 34 (39) (2024) 2403245.

[43] Z.Y. Wang, X. Wang, X.Y. Dai, T.M. Xu, X.Q. Qian, M.Q. Chang, Y. Chen, 2D catalytic nanozyme enables cascade enzyodynamic effect-boosted and Ca^{2+} overload-induced synergistic ferroptosis/apoptosis in tumor, Adv. Mater. 36 (24) (2024) 2312316.

[44] X.R. Yang, H. Zhang, Z.H. Wu, Q. Chen, W. Zheng, Q.Y. Shen, Q.L. Wei, J.W. Shen, Y. Guo, Tumor therapy utilizing dual-responsive nanoparticles: A multifaceted approach integrating calcium-overload and PTT/CDT/chemotherapy, J. Control. Release 376 (2024) 646–658.

[45] Y.X. Xiao, J.M. Yin, P. Liu, X. Zhang, Y.J. Lin, J. Guo, Triptolide-induced cuproptosis is a novel antitumor strategy for the treatment of cervical cancer, Cell. Mol. Biol. Lett. 29 (1) (2024) 00623.

[46] X.A. Chen, C. Xu, P. Zhao, Y. Zhang, J.Z. Guo, X.L. Hu, H. Gao, C.N. Zhang, X. W. Qu, J.M. Zhang, A multichannel Ca^{2+} nanomodulator amplifies exogenous and endogenous calcium overload for efficient antitumor and antimetastasis therapy, Chem. Eng. J. 463 (2023) 142478.

[47] J.F. Zhang, X.F. Yin, C.C. Li, X.L. Yin, Q.H. Xue, L. Ding, J.L. Ju, J.F. Ma, Y. Zhu, D. S. Du, R.L. Reis, Y.L. Wang, A multifunctional photoacoustic/fluorescence dual-mode-imaging gold-based theranostic nanoformulation without external laser limitations, Adv. Mater. 34 (19) (2022) 2110690.

[48] X. Pan, A.T. Gao, Y.N. Hu, Z.Y. Hu, C. Xie, Z.T. Lin, Gadolinium-containing semiconducting polymer nanoparticles for magnetic resonance/fluorescence dual-modal imaging and photothermal therapy of oral squamous cell carcinoma, Nano Res. 16 (2) (2022) 2808–2820.

[49] R. Rodriguez, S. Müller, L. Colombeau, S. Solier, F. Sindikubwabo, T. Cañeque, Metal ion signaling in biomedicine, Chem. Rev. 125 (2025) 660–744.

[50] F.Y. Shen, Y. Fang, Y.J. Wu, M. Zhou, J.F. Shen, X.Q. Fan, Metal ions and nanometallic materials in antitumor immunity: Function, application, and perspective, J. Nanobiotechnol. 21 (2023).